Cellular/Molecular

# EHBP1 Is Critically Involved in the Dendritic Arbor Formation and Is Coupled to Factors Promoting Actin Filament Formation

**Yuanyuan Ji, Maryam Izadi-Seitz, Annemarie Landmann, Lukas Schwintzer, Britta Qualmann, and Michael M. Kessels**
Institute of Biochemistry I, Jena University Hospital/Friedrich Schiller University Jena, 07743 Jena, Germany

**The coordinated action of a plethora of factors is required for the organization and dynamics of membranous structures critically underlying the development and function of cells, organs, and organisms. The evolutionary acquisition of additional amino acid motifs allows for expansion and/or specification of protein functions. We identify a thus far unrecognized motif specific for chordata EHBP1 proteins and demonstrate that this motif is critically required for interaction with syndapin I, an F-BAR domain-containing, membrane-shaping protein predominantly expressed in neurons. Gain-of-function and loss-of-function studies in rat primary hippocampal neurons (of mixed sexes) unraveled that EHBP1 has an important role in neuromorphogenesis. Surprisingly, our analyses uncovered that this newly identified function of EHBP1 did not require the domain responsible for Rab GTPase binding but was strictly dependent on EHBP1's syndapin I binding interface and on the presence of syndapin I in the developing neurons. These findings were underscored by temporally and spatially remarkable overlapping dynamics of EHBP1 and syndapin I at nascent dendritic branch sites. In addition, rescue experiments demonstrated the necessity of two additional EHBP1 domains for dendritic arborization, the C2 and CH domains. Importantly, the additionally uncovered critical involvement of the actin nucleator Cobl in EHBP1 functions suggested that not only static association with F-actin via EHBP1's CH domain is important for dendritic arbor formation but also actin nucleation. Syndapin interactions organize ternary protein complexes composed of EHBP1, syndapin I, and Cobl, and our functional data show that only together these factors give rise to proper cell shape during neuronal development.**

*Key words:* **actin nucleator Cobl; cooperative function; dendritic arbor formation; F-BAR domain protein syndapin; functional ternary complexes; neuronal EHBP1 functions**

### Significance Statement

**The development and function of cells, organs, and organisms requires proper organization and dynamics of membranous structures dependent on the coordinated action of a plethora of factors. We here identify a motif specific for EHBP1 proteins from chordates that is critically required for interaction with syndapin I, a neuronal membrane-shaping protein. Functional studies unraveled a thus far unrecognized important role of dendritic arbor formation in developing neurons and that this function strictly depends on syndapin I. EHBP1 accumulated together with syndapin I, the actin nucleator Cobl, and F-actin at nascent dendritic branch sites. Syndapin interactions organize ternary EHBP1/syndapin I/Cobl complexes, and functional examinations reveal that only together these factors give rise to proper cell shape during neuronal development.**

Received Feb. 7, 2023; revised Dec. 1, 2023; accepted Dec. 5, 2023.

Author contributions: Y.J., M.I.-S., A.L., L.S., B.Q., and M.M.K. analyzed data; Y.J., M.I.-S., A.L., and L.S. performed research; B.Q. and M.M.K. designed research; B.Q. and M.M.K. wrote the paper.

We thank A. Kreusch, K. Gluth, B. Schade, M. Öhler, and N. Ulrich for their excellent technical support. This work was partially supported by *DFG* grants KE685/7-1 to MMK and QU116/9-1 to B.Q.

The authors declare no competing financial interests.

Correspondence should be addressed to Britta Qualmann at britta.qualmann@med.uni-jena.de or Michael M. Kessels at michael.kessels@med.uni-jena.de

https://doi.org/10.1523/JNEUROSCI.0236-23.2023



## Introduction

Organization and dynamics of membranous structures are key for the development and function of cells, organs, and organisms and involve the coordinated action of a plethora of factors. EHBP1 has been originally identified in mammalian cells as an interaction partner of the membrane trafficking protein EHD2 (Guilherme et al., 2004a). Since then, a comparatively low number of studies described rather diverse functional implications of EHBP1 in mammalian cells and model organisms such as

*C. elegans* and *Drosophila melanogaster*. In mammalian cell lines, EHBP1 knockdown affected transferrin internalization as well as insulin-stimulated GLUT4 recycling (Guilherme et al., 2004a, b). In a hepatoma cell line, EHBP1 was shown to be important for autophagic lipid droplet engulfment (Li et al., 2016). In *C. elegans*, EHBP1 loss-of-function mutants exhibited defects of endosomal morphology and cargo localization. Worms subjected to EHBP1 siRNA also displayed an impaired trafficking of membrane proteins in intestinal, neuronal, and germline cells (Shi et al., 2010). Drosophila EHBP1 was demonstrated to regulate exocytosis and recycling of the Notch-ligand Delta (Giagtzoglou et al., 2012) and the secretion of scabrous (a positive regulator of Notch signaling) in the developing eye (Giagtzoglou et al., 2013). In fly photoreceptor cells, EHBP1 was also found to be involved in the polarized transport of $Na^+K^+$-ATPase at *trans*-Golgi stacks (Nakamura et al., 2020). A localization of EHBP1 to caveolae at the plasma membrane of different non-neuronal cells added to the diverse proposed functions of EHBP1 in different species and cell types (Matthaeus et al., 2022). An association of EHBP1 with different forms of cancer also was described (Gudmundsson et al., 2008; Matsumoto et al., 2021). These surprisingly diverse observations may be attributable to the low degree of conservation between EHBP1 proteins from different species (Shi et al., 2010). Notably, fly and worm EHBP1 proteins completely lack NPF motifs mediating EH domain interactions.

For several vesicular trafficking-related functions of EHBP1, complex formation with distinct Rab family members via a C-terminal bMERB (bivalent Mical/EHBP Rab binding) domain was reported to be important. Among several Rab subfamily members found to be associated with EHBP1 (Rai et al., 2016, 2020), EHBP1 seems to particularly cooperate with Rab10. In several cases, phenocopies between EHBP1 and Rab10 loss-of-function were reported (Shi et al., 2010; Li et al., 2016; Wang et al., 2016; Nakamura et al., 2020; Farmer et al., 2021). However, the Notch signaling effects of EHBP1 rather were Rab11-mediated (Giagtzoglou et al., 2012).

A central calponin homology (CH) domain in EHBP1 proteins mediates binding to actin filaments, and this was promoted by Rab10 presence (Wang et al., 2016). The CH domain forms intramolecular complexes with the bMERB domain autoinhibiting efficient F-actin binding (Rai et al., 2020). In addition to potential membrane recruitment via EHD and/or Rab proteins, EHBP1 proteins also are characterized by an N-terminal C2 domain binding to different negatively charged phospholipids as reported for human and worm EHBP1 (Wang et al., 2016; Rai et al., 2020) and a C-terminal CaaX box. This target for farnesylation (Rai et al., 2020), however, is absent in *C. elegans* EHBP1. Thus, EHBP1 functions appear to largely depend on subcellular localization as well as on cellular and organismic context. Recently, markers in *EHBP1* were reported to show genome-wide significant evidence of association with a delayed recall memory phenotype in gene-based analyses (Homann et al., 2022) suggesting some, so far unrecognized functions of EHBP1 in the brain.

We here identify EHBP1 as a novel binding partner of syndapin I, an F-BAR domain membrane-shaping protein predominantly expressed in neurons (Qualmann et al., 1999; Itoh et al., 2005; Dharmalingam et al., 2009; Koch et al., 2011) and uncover functions for EHBP1 in neuronal development. Surprisingly, while these functions of EHBP1 critically depended on syndapin I and the highly conserved syndapin interaction motif of EHBP1, they did not require the domain responsible for Rab GTPase binding.

## Material and Methods

*DNA constructs.* Rat EHBP1 isoforms were cloned from rat brain and heart cDNAs, respectively. The N-terminal parts of EHBP1 isoforms were cloned with 5′-atctcgagatggcttcagtttgg-3′ as forward primer and 5′-ttacaggctgaagctttttgc-3′ as reverse primer. The PCR products were inserted into pEGFP-C3 (Clontech) using XhoI and HindIII. The internal HindIII site of EHBP1 (at position aa722; numbers according to isoform X1) was also used for fusion with the C-terminal part of EHBP1 cloned using 5′-gcaaaagcttcagcctgtaa-3′ as forward and 5′-ttcccgggctactgaagagtgc-3′ as reverse primer. Obtained were rat EHBP1 isoform X1 (from the brain; XP_017454733) and rat EHBP1 isoforms lacking aa213–247 and aa879–914 of isoform X1 (corresponding to either isoform X3 (Δ213–247), X4 (Δ879–914) and/or X7 (Δ213–247 + Δ879–914) from the heart.

Rat cDNAs from different tissues (mixed sex) were obtained according to the procedures described (Haag et al., 2012). In brief, tissue samples were dissected and snap-frozen in liquid nitrogen. After grinding in liquid nitrogen, the samples were resuspended in Trizol reagent (Invitrogen) and then treated with RNAse-free DNAse (Qiagen). The isolated mRNA was then reverse transcribed using oligo-dT primers and RevertAid H Minus Reverse Transcriptase (Fermentas).

GST-EHBP1$^{267–394}$- and GST-EHBP1$^{267–529}$-encoding plasmids were generated by PCR using rat EHBP1 isoform X1 as template and insertion into pGEX-6P (GE Healthcare).

Human EHBP1 isoform 2 was obtained in the form of the IMAGE clone 6502257. Similar to the rat EHBP1 isoform X3 (Δ213–247), human EHBP1 isoform 2 lacks 35 amino acids when compared to isoform 1 (for overview, see Fig. 1-1 and Fig. 1-2). The isoform 2 deletion mutants human EHBP1$^{1–688}$ and EHBP1$^{231–389}$ were generated by PCR using IMAGE clone 6502257 as a template (aa231–389 of isoform 2 correspond to the sequence aa266–424 of isoform 1).

EHBP1 RNAi [target site encodes aa510–516 (human EHBP1; NP_056067), aa490–496 (rat EHBP1; XP_017454733), and aa520–526 (mouse EHBP1; NP_001239444), respectively] was generated by subjecting the forward primer 5′-gatccggatttgccagcattggaattttgatatccgaattccaatgctggcaaatccttttttta-3′ and the reverse primer 5′-agcttaaaaaaggatttgccagcattggaattcggatatcaaaattccaatgctggcaaatccg-3′ to primer annealing, phosphorylation, and subcloning into pRNAT-H1.1/Hygro-GFP (GenScript) using its BamH1 and HindIII sites. pRNAT-H1.1/Hygro-GFP plasmid expressing a scrambled RNAi sequence was as described (Ahuja et al., 2007; Ji et al., 2021). As the RNAi targeting site is located in the CH domain-encoding region, all relevant splice isoforms of rat EHBP1 known thus far (compare also Fig. 1-1) are targeted.

RNAi tools for validation of knockdown were generated by replacing the GFP reporter of pRNAT-H1.1 with full-length, GFP-tagged rat EHBP1. Alternative pRNAT constructs for knockdown validations contained GFP-EHBP1$^{399–722}$, which was obtained by subcloning an ApaI/ApaI fragment of rat GFP-EHBP1$^{1–722}$ first into pEGFP-C3 using the internal ApaI site of EHBP1 (position aa399) as well as the ApaI site of the pEGFP-C3 MCS and then subcloning the resulting GFP-EHBP1$^{399–722}$-encoding sequence into pRNAT-H1.1 vectors using the NheI and SmaI sites of pRNAT and thereby replacing the GFP reporter of pRNAT-H1.1. The GFP-EHBP1- and GFP-EHBP1$^{399–722}$-expressing pRNAT vectors for RNAi validation either contained EHBP1 RNAi, a scrambled (Scr.) RNAi, or lacked any insertion into the MCS under the H1.1 promotor.

Plasmids for rescue attempts were built by replacing the GFP reporter with either RNAi-insensitive GFP-tagged rat EHBP1 (EHBP1 RNAi/EHBP1* and scrambled RNAi/EHBP1*) or by mutant GFP-EHBP1* sequences. RNAi-insensitive EHBP1 (EHBP1*) was obtained by introducing silent mutations into the RNAi target site using 5′-tacgatggattcgcgtctataggtatttcccgcttac-3′ as forward primer and 5′-gtaagcgggaaatacctatagacgcgaatccatcgta-3′ as reverse primer and insertion into pEGFP.

For additional rescue attempts and biochemical analyses, several rat (isoform X1) EHBP1 deletion mutants, that is, GFP-EHBP1*$^{\Delta C2}$ (Δaa2–158), GFP-EHBP1*$^{\Delta KRAP}$ (ΔKRRAPAPP; Δaa371–378;

replacement by EcoRI site), GFP-EHBP1*$^{\Delta CH}$ (Δaa422–528; replacement by EcoRI site), and GFP-EHBP1*$^{\Delta bMERB}$ (Δaa1029–1205), were generated by PCR using the corresponding primers and the internal Hind III site of rat EHBP1 for combination with the corresponding, unchanged half of the EHBP1* sequence and cloning into pEGFP-C3. Subsequently, the sequences encoding for the GFP-tagged, RNAi-resistant mutants were subcloned into EHBP1 RNAi- and Scr. RNAi-encoding plasmids, respectively, replacing the GFP sequence of pRNAT.

Plasmids encoding for GST-tagged syndapin I full-length and SH3 domain (aa376–441), respectively, were described previously (Qualmann et al., 1999; Qualmann and Kelly, 2000). A plasmid for the generation of recombinant, untagged syndapin I full-length was also described recently (Izadi et al., 2021). Plasmids encoding for Flag-syndapin I (Kessels and Qualmann, 2006), Xpress-syndapin I (Kessels and Qualmann, 2002), (Flag-tagged) mCherry-syndapin I (Hou et al., 2015), and mitochondrially targeted syndapin I (Mito-mCherry-SdpI) and syndapin I ΔSH3 (Mito-mCherry-SdpI$^{\Delta SH3}$; Schneider et al., 2014) were as previously published. Syndapin I RNAi (driven by pRNAT-H1.1) was validated for successful knockdown (Dharmalingam et al., 2009) and for specificity via rescue experiments in phenotypical analyses using silently mutated, RNAi-insensitive syndapin I (Schneider et al., 2014). CherryF coexpression was used as a reporter as described before (Schneider et al., 2014).

Plasmids encoding for GST-tagged syndapin II isoforms (II-s and II-l) were as described (Qualmann and Kelly, 2000). Plasmids encoding for Flag-syndapin II-s (Dharmalingam et al., 2009) and Flag-syndapin III (Izadi et al., 2021) were reported before, too.

Plasmids encoding for GST-EHD1 and GST-EH domain of EHD1 were as described (Braun et al., 2005).

A GFP-N-WASP$^{265–501}$-encoding plasmid was generated by PCR using already described rat N-WASP template and primers (Kessels and Qualmann, 2002) and insertion of the PCR product into pEGFP-C1. N-WASP RNAi (driven by pRNAT-H1.1; CherryF coexpression) was described before (Pinyol et al., 2007; Schneider et al., 2014).

GFP-Cobl, GFP-Cobl$^{1–408}$, and GFP-Cobl-like$^{1–457}$ were as described (Ahuja et al., 2007; Izadi et al., 2021). Cobl RNAi plasmids (RNAi#1) coexpressing CherryF as reporter were generated accordingly by replacing the GFP reporter sequence of the published Cobl RNAi plasmid (Ahuja et al., 2007) by the CherryF sequence (Izadi et al., 2021).

LifeAct-RFP for the detection of F-actin time-lapse imaging was described (Hou et al., 2015).

Correct cloning by PCR was verified by sequencing in all cases.

*Antibodies, reagents, and proteins.* Polyclonal rabbit anti-EHBP1 antibodies (RRID AB_2097216) were from Proteintech. Rabbit and guinea pig anti-syndapin I antibodies and affinity purification procedures were described previously (Qualmann et al., 1999; Braun et al. 2005; Koch et al., 2011). Anti-GST antibodies from guinea pigs were described before as well (Qualmann and Kelly, 2000). Rabbit anti-GST antibodies were generated and purified as described (Qualmann et al., 1999; Izadi et al., 2021).

Polyclonal guinea pig anti-MAP2 antibodies (RRID AB_2138181), guinea pig anti-homer1 antibodies (RRID AB_10549720), and mouse anti-synaptophysin antibodies (RRID AB_887824) were from Synaptic Systems. Monoclonal mouse anti-β-actin antibodies (RRID AB_476744) were from Sigma, polyclonal goat anti-GAPDH antibodies (RRID AB_1563046) were from Santa Cruz Biotechnology, and mouse anti-COX IV (RRID AB_301443) and anti-cytochrome *c* antibodies (ab3255; no RRID available) were from Abcam. Phalloidin Alexa Fluor 568 was from Thermo Fisher Scientific (A12380; no RRID available).

Polyclonal rabbit anti-GFP was from Abcam (RRID AB_303395). Monoclonal mouse anti-GFP antibodies (JL-8) were from Clontech (RRID AB_10013427). Monoclonal mouse anti-Flag (M2; RRID AB_259529) antibodies and polyclonal rabbit anti-Flag antibodies (RRID AB_439687) were from Sigma-Aldrich. Anti-Xpress antibodies were from Invitrogen (RRID AB_2556552).

Secondary antibodies used included Alexa Fluor 568-labeled goat anti-guinea pig antibodies (RRID AB_141954), Alexa Fluor 647-labeled donkey anti-mouse antibodies (RRID AB_162542), Alexa Fluor 647-labeled goat anti-mouse antibodies (RRID AB_141725), Alexa Fluor 488 donkey anti-rabbit (RRID AB_2535792) antibodies, DyLight 800-conjugated goat anti-rabbit (RRID AB_2556775), and DyLight 800 goat anti-mouse antibodies (RRID AB_2556774) from Molecular Probes and Thermo Fisher Scientific, respectively. Donkey anti-guinea pig antibodies coupled to IRDye680 and IRDye800, respectively, were from LI-COR Bioscience (RRID AB_10956079 and RRID AB_1850024). Alexa Fluor 647-labeled donkey anti-guinea pig (RRID AB_2340476), as well as peroxidase-conjugated goat anti-rabbit and anti-guinea pig antibodies were from Jackson ImmunoResearch, respectively (RRID AB_2337945; RRID AB_2337405).

GST-tagged fusion proteins were purified from *E. coli* lysates using glutathione agarose or sepharose (Sigma-Aldrich; GenScript) as described previously (Qualmann and Kelly, 2000; Schwintzer et al., 2011). After purification, fusion proteins were dialyzed against PBS, characterized by SDS-PAGE, and snap-frozen and stored at −80°C.

Tag-free syndapin I was generated by expression in *E. coli* (pGEX-6P vector; GE Healthcare) and GST tag cleavage from purified GST-syndapin I using PreScission protease (GE Healthcare) according to procedures described previously (Izadi et al., 2021).

*EHBP1 RNAi validation and coprecipitation of proteins using lysates of transfected HEK293 cells.* Culturing of HEK293 cells (RRID CVCL_0045) and transfection using TurboFect (Thermo Fisher Scientific) was essentially done as described (Haag et al., 2012). The cell line was regularly tested for mycoplasma and was mycoplasma-negative.

Lysates of transfected HEK293 cells were generated as described (Kessels and Qualmann, 2006; Izadi et al., 2021). In brief, HEK293 cells were transfected, washed with PBS 24–48 h after transfection, harvested and subjected to sonification for 10 s, and/or lyzed by incubation with lysis buffer [10 mM HEPES pH 7.4, 0.1 mM $MgCl_2$, 1 mM EGTA, 1% (v/v) Triton X-100] containing 150 mM NaCl and EDTA-free protease inhibitor cOmplete (Roche) for 30 min at 4°C. Cell lysates were obtained as supernatants from centrifugations at 20,000 × *g* (20 min at 4°C).

Coprecipitation experiments with extracts from HEK293 cells expressing different GFP-fusion proteins were essentially performed as described before (Qualmann et al., 1999; Schwintzer et al., 2011). In brief, HEK293 cell lysates were incubated with purified, recombinant GST fusion proteins immobilized on glutathione sepharose beads (GenScript) for 3 h at 4°C. The reactions were then washed several times with lysis buffer containing 150 mM NaCl and EDTA-free protease inhibitor cOmplete. Bound protein complexes were subsequently eluted with 20 mM reduced glutathione, 120 mM NaCl, and 50 mM Tris/HCl pH 8.0 (30 min RT) or obtained by incubating the beads in 4× SDS sample buffer at 95°C for 5 min.

Samples were analyzed by SDS-PAGE and (quantitative) fluorescent Western blotting using a LI-COR Odyssey System (LI-COR).

*Ternary complex examinations.* Coprecipitations of three protein partners were essentially performed according to Izadi et al. (2021). In brief, the possibility of complex formations of EHBP1, syndapin I, and either N-WASP, Cobl-like, or Cobl in ternary complexes was experimentally addressed by using purified, immobilized GST-EHBP1$^{267–394}$, purified untagged syndapin I (putative bridging component; for preparation procedures, see above), and GFP-Cobl$^{1–408}$, GFP-Cobl-like$^{1–457}$, and GFP-N-WASP$^{265–501}$ (syndapin binding partners; offered in form of lysates of transfected HEK293 cells; see above). Ternary complex examinations were essentially performed as the coprecipitation studies described above (using a lysis buffer containing 150 mM NaCl) except that the lysates of HEK293 cells were not only incubated with immobilized GST-EHBP$^{267–394}$ but also with tag-free syndapin I (0.1 mg/sample) for 3 h at 4°C.

After washing with lysis buffer containing 150 mM NaCl, bound proteins were eluted with 20 mM reduced glutathione, 120 mM NaCl, and 50 mM Tris/HCl pH 8.0. Eluates and supernatants were separated by SDS-PAGE and analyzed by anti-syndapin I, anti-GST, and anti-GFP immunoblotting.

*Heterologous coimmunoprecipitation analyses.* Heterologous coimmunoprecipitations were essentially conducted as described (Hou et

al., 2018). In brief, HEK293 cells cotransfected with Flag-tagged syndapin I, syndapin II, and syndapin III, respectively, and GFP-tagged EHBP1 proteins were extracted with lysis buffer containing 50 mM NaCl and protease inhibitor cOmplete and incubated at 4°C for 2 h with 5 µg murine anti-GFP antibodies and with 5 µg with murine unrelated IgG (Santa Cruz Biotechnology), respectively.

Subsequently, 15 µl of a suspension [1:2 (v/v) in lysis buffer) of protein A/G-agarose (Santa Cruz Biotechnology)] was added to each sample, incubated for another 3 h, and then isolated by centrifugation. Protein/antibody complexes bound to the agarose were then washed three times with lysis buffer, eluted with 2× SDS sample buffer, and then analyzed by immunoblotting using rabbit anti-GFP antibodies for detection of immunoprecipitated proteins and anti-Flag antibodies for detection of coimmunoprecipitated GFP-fusion proteins.

*Generation of lysates of different murine tissues.* Different organs and tissues were prepared from adult mice, cut into small pieces and homogenized in a 1:6 (w/v) ratio with ice-cold RIPA buffer [50 mM Tris/HCl pH 8.0, 150 mM NaCl, 1% (v/v) NP-40%, 0.5% (v/v) desoxycholate, 0.1% (w/v) SDS] including 1 mM EDTA using an Ultra Turrax (Ika Ultra Turrax T5Fu; 20,000 rpm, 10 s). Cell debris and nuclei were removed by centrifugation at 10,000 × *g* (15 min; 4°C).

Developmental expression patterns were analyzed using brains from embryonic, neonatal, and juvenile mice at the following ages, E16, E18, P0, P4, P8, P12, 4 weeks, and 8 weeks. The animals were sacrificed and the brains were isolated, cut into pieces, and homogenized in a 1:10 (w/v) ratio in brain homogenization buffer (0.32 M sucrose, 1 mM EDTA and 5 mM HEPES pH 7.4 containing the EDTA-free protease inhibitor cOmplete using a potter (Potter S; Sartorius). Cell debris and nuclei were removed by centrifugation at 10,000 × *g* (15 min; 4°C).

Protein concentrations were determined by bicinchoninic acid assays (Pierce) and samples corresponding to equal amounts of total protein were analyzed by immunoblotting.

*Culturing and lysate preparation of cortical neurons and glia cells from mice.* Neuronal cultures for Western blot analyses were prepared from cortices of P0 mouse pups essentially as described for rat cortical neuron cultures (Wolf et al., 2019). The neurons were maintained at 37°C with 90% humidity and 5% $CO_2$.

At DIV5, cultured cortical neurons were washed with PBS, harvested by scraping, sonicated for 10 s, and lyzed for 20 min at 4°C in lysis buffer containing 150 mM NaCl and the EDTA-free protease inhibitor cOmplete. Cell lysates were then obtained as centrifugation supernatants (20,000 × *g*; 10 min; 4°C).

Mixed glia cell cultures were obtained from P0 mouse brains, from which the olfactory bulb, the cerebellum, and the brainstem had been removed. The brains were dissociated in the cerebral hemispheres and the midbrain. Meninges and blood vessels were carefully removed. The cerebral hemispheres and midbrain tissues were pooled and triturated in Dulbecco's modified Eagle's medium/Nutrient Mixture F-12 (DMEM/F-12) by slowly passing the tissue through a 10 ml serological pipette until the tissues were smaller than the opening of a 1 ml pipette tip. The suspension was then trituated further through a 1 ml pipette tip until the tissue pieces were smaller than the opening of a 200 µl pipette tip and then four times more through a 200 µl pipette tip. The suspension was then strained through a 70 µm cell strainer and centrifuged at 430×g for 6 min at 4°C. The supernatant was removed, and the cells were resuspended in warm DMEM/F-12 containing 10% (v/v) FBS, nonessential amino acids, 1 mM sodium pyruvate, and 2 mM L-glutamine as well as 50 U/mlpenicillin and 50 µM streptomycin, counted and seeded into flasks. The cells were maintained at 37°C with 90% humidity and 5% $CO_2$, and the medium was replaced every 3 d. Cells were harvested and lyzed for immunoblotting 2 weeks after seeding.

*Subcellular fractionation of rat brain homogenates.* Rat brain tissue fractionations were essentially performed as described (Carlin et al., 1980; Qualmann et al., 2004) with slight modifications. Brain material (adult; female) was cut into small pieces and homogenized by 12 potter strokes in an ice-cold brain homogenization buffer. Cell debris and nuclei (P1) were separated by 1,000 × *g* centrifugation for 10 min at 4°C from the low-speed supernatant (S1). P1 was resuspended in brain homogenization buffer, subjected to 12 potter strokes again, and centrifuged at 1,000 × *g* to yield S1′ and P1′. S1 and S1′ were combined and centrifuged at 12,000 × *g* for 15 min. The pellet of the 12,000 × *g* centrifugation (P2) was resuspended and homogenized (six strokes in the potter) and centrifuged again at 12,000 × *g* for 20 min leading to P2′ and S2′. S2′ was combined with the above supernatant S2 and subjected to ultrahigh-speed centrifugation (UC; 100,000 × *g* for 1 h) yielding the UC pellet (microsomes) and the corresponding supernatant (UC supernatant).

The washed pellet P2′ obtained by the 12,000 × *g* centrifugation step represents a crude membrane fraction and was fractionated further using a 0.85/1.0/1.2 M sucrose step gradient. The fractions of myelin, light membranes, and synaptosomes were isolated at the borders of the different sucrose concentrations, and mitochondria were isolated as the pellet.

Synaptosomes were subsequently subjected to osmotic shock and extraction in 1 mM Tris/HCl, pH 8.1, for 30 min. Centrifugation at 33,000 × *g* for 30 min yielded the synaptic membrane fraction as a pellet.

Samples of the different fractions corresponding to either 2.5 or 5 µg protein content were separated by SDS-PAGE and analyzed by immunoblotting.

*Coprecipitation of endogenous EHBP1 or syndapin I from rat brain lysates.* For coprecipitation of endogenous EHBP1 or syndapin I, brain lysates were prepared from rats sacrificed by cervical dislocation as described (Schwintzer et al., 2011; Izadi et al., 2021). Extracts were prepared in lysis buffer containing EDTA-free protease inhibitor cOmplete and 150 mM NaCl using a potter (12 strokes). After 1,000 × *g* centrifugation for 20 min, the supernatants were used for coprecipitation analyses of endogenous proteins.

For coprecipitation of endogenous EHBP1, purified, recombinant GST-syndapin I and GST-syndapin I SH3 fusion proteins were used, and for endogenous syndapin I, GST-EHBP1$^{267–394}$ and GST-EHBP1$^{267–529}$ were employed. GST served as a specificity control. The proteins were immobilized on glutathione sepharose and incubated with the prepared rat brain lysates for 3 h at 4°C.

After washing, bound proteins were eluted in sample buffer, subjected to SDS-PAGE, and analyzed by anti-EHBP1 and anti-syndapin I immunoblotting, respectively.

*Endogenous coimmunoprecipitation of EHBP1 and syndapin I from rat brain lysates.* Rat brain lysates were prepared in Triton X-100-free lysis buffer containing 50 mM NaCl and protease inhibitors using a potter. After the addition of Triton X-100 [1% (v/v) final], the samples were centrifuged at 1,000 × *g* for 20 min at 4°C. The resulting supernatants were incubated for 2.5 h with affinity-purified rabbit anti-syndapin I antibodies and non-immune rabbit IgGs, respectively. After 2 h of incubation at 4°C, the antibodies and associated proteins were isolated with protein A/G PLUS agarose, washed with ice-cold lysis buffer with 50 mM NaCl and protease inhibitors, eluted with SDS sample buffer (95°C, 5 min), and analyzed by immunoblotting using anti-syndapin I and anti-EHBP1 antibodies.

*Culturing, transfection, and immunostaining of primary rat neurons.* Rat hippocampal neurons (rat strain, Wistar) were prepared and cultured until day in vitro (DIV) 4 as described (Wolf et al., 2019; Izadi et al., 2021). In brief, neurons isolated from hippocampi of E18 rats (of mixed sex) were seeded at densities of 60,000/well (24-well plate) and cultured in Neurobasal medium containing 2 mM L-glutamine, 1× B-27, and a mixture of 100 U/ml penicillin and 100 µg/ml streptomycin (Invitrogen). The neurons were maintained at 37°C with 90% humidity and 5% $CO_2$.

The neurons were transfected with 1 µl Lipofectamine 2000 and 1 µg DNA per well in antibiotic-free medium in 24-well plates. After 4 h, the transfection medium was replaced by a conditioned medium.

After 40 h, neurons were fixed by 4% (w/v) paraformaldehyde (PFA) for 5–7 min. After permeabilization and blockage by blocking solution consisting of 10% (v/v) horse serum, 5% (w/v) bovine serum albumin,

and 0.2% (v/v) Triton X-100 in PBS for 1 h at RT, the samples were immunostained with primary antibodies, washed three times with blocking solution, and then incubated with secondary antibodies and DAPI. After washing, the coverslips were mounted onto glass slides using Moviol.

Similar procedures were applied for immunofluorescence analyses of untransfected neurons.

*Imaging and quantitative assessments of neuronal morphology.* The transfected neurons from 2–4 independent assays were imaged by systematic sweeps across the coverslips using a Zeiss Axio Observer Z1 microscope/Apotome (objectives, Plan-Apochromat 100×/1.4, 63×/1.4, 40×/1.3, and 20×/0.5) and an AxioCam MRm CCD camera (Zeiss). Digital images were recorded by ZEN2012 (RRID SCR_013672). Image processing was done by Adobe Photoshop (RRID SCR_014199).

Morphometric measurements were based on anti-MAP2 immunosignals to identify dendrites of neurons. Neuronal morphologies were reconstructed in 3D using Apotome image stacks processed by Imaris 8.4.0 software (RRID SCR_007366) using the following settings: thinnest diameter and gap length, both 2 µm, and minimum segment length, 10 µm.

The number of dendritic branching points, terminal points, total dendritic tree length, and Sholl intersections was analyzed as described (Ji et al., 2021). Additionally, branch depth levels (with level 1 representing primary dendrites) were determined using Imaris 8.4.0.

*3D time-lapse analyses of developing primary hippocampal neurons and examinations of protein accumulations at dendritic branch sites.* Primary hippocampal neurons for live imaging were prepared as described above except that the medium was replaced by Neurobasal-A medium (Invitrogen) supplemented with 0.5 mM L-alanyl-L-glutamine, 0.025 mM L-glutamate, B-27 supplement, and penicillin/streptomycin 1 h after seeding of the cell suspension. The neurons were transiently transfected with Lipofectamine 2000 at DIV6, as described (Hou et al., 2015; Izadi et al., 2018).

Protein dynamics were tracked in relation to dendritic branch development by 3D time-lapse imaging essentially done as described (Izadi et al., 2018, 2021, 2023). In brief, the medium was replaced by a live imaging buffer adjusted to osmolarity with a freezing point osmometer (Osmomat 3000; Gonotec), and the developing neurons were imaged 14–26 h after transfection using a spinning disc microscope to ensure fast 3D recordings with minimal phototoxicity. The time-lapse imaging was done in an open coverslip holder in an incubator built around the spinning disc microscope. Images were recorded using a C-Apochromat objective (63×/1.20 W Korr M27) and a QuantEM 512SC EMCCD camera. Images were taken as *z*-stacks of 7–20 images (depending on cellular morphology) with *z*-intervals of 0.31 µm. Time intervals were set to 10 s, and exposure times were 50–200 ms. Laser power was kept between 3 and 10%.

Images were processed using ZEN2012, Imaris, ImageJ (RRID SCR_003070), and Adobe Photoshop, respectively.

Quantitative evaluations of protein dynamics were determined as described before (Izadi et al., 2021, 2023). In brief, the degree of accumulation of EHBP1, syndapin I, Cobl, and LifeAct (for F-actin tracking) fused to fluorescent proteins as well as for mCherry as control was determined at dendritic branch initiation sites (morphologically defined by subsequent branch formation) for each imaging frame prior to and at protrusion start, which was defined as $t = 0$. The maximal fluorescence intensity was identified for each dendritic branch induction site and normalized to a neighboring non-branching control ROI at the same dendrite.

For spatiotemporal analyses, the time points of the frames with the highest accumulation of the proteins of interest in the time window of 1 min prior to protrusion induction were averaged. In the rare case that two maxima of equal intensity occurred prior to branch initiation, both time values were considered and averaged.

*Statistical analyses and sample size estimation.* No explicit power analyses were used to compute and predefine required sample sizes. Instead, all neuronal analyses were conducted by systematic sampling of transfected cells across coverslips to avoid any bias in cell imaging.

All quantitative morphological data were obtained from 2–4 independent neuronal preparations. Each of these assays contained several independent coverslips for each condition of transfection and immunostaining. For each condition, minimal *n* numbers of 20 individual neurons per assay were aimed for. Higher *n* numbers yielded from the systematic imaging were accepted. Outliers or strongly scattering data were considered as reflecting the biological variance and were thus not excluded from the analyses.

All *n* numbers of quantitative analyses are reported directly in the figures of the manuscript. All *n* numbers represent independent biological samples (i.e., neurons; branch induction sites) or biochemical assays (quantitative RNAi validation experiments; Fig. 6*A*,*B*). Technical replicates to minimize measurement errors were not useful because technical errors were small in relation to the biological/biochemical variances observed.

All additional data (Western blots, immunofluorescence pictures) shown are representative examples. All non-quantitative experiments were reproduced at least once.

Quantitative data represent mean ± SEM throughout the manuscript. Quantitative biochemical data (Fig. 6*A*,*B*) and live imaging data (Figs. 5, 11) are provided as bar and dot plot overlays. Due to the relatively few individual data points of such analyses, this type of presentation is most suitable to report the data distribution around the mean.

Normal data distribution and statistical significance were tested using GraphPad Prism 6 software (RRID SCR_002798). The statistical tests employed are reported in the respective figure legends.

The numbers of dendritic branching points, the numbers of terminal points, and total dendritic lengths were analyzed for statistical significance using either Student's *t* test (Fig. 6*D*–*F*) or one-way ANOVA and Tukey's posttest (Figs. 3, 4, 7, 8, 10, 12). All Sholl analyses as well as all branch depth analyses were tested by two-way ANOVA and Sidak posttest.

Live imaging data were obtained from transfected cells of 2-5 independent neuronal preparations and analyzed for statistical significance using either the Mann–Whitney *U* test (Fig. 5*B*) or one-way ANOVA and Tukey's posttest (Fig. 11*B*).

Statistical significances were marked by * $p < 0.05$, ** $p < 0.01$, *** $p < 0.001$, and **** $p < 0.0001$ throughout. In addition, the numbers of *p* values are reported directly in the figures (except for Sholl and branch depth analyses). Note that for $p < 0.0001$ (****), no values were provided by the software Prism 6, as the *p* values are too small.

*Ethics statement.* As exclusively cells and tissue samples isolated from postmortem WT animals were used in this study, neither permission for animal experiments nor breeding permission for genetically modified animals (*Zuchtrahmenantrag*) was required.

Rats and mice used to obtain biological material were of either sex and bred by the animal facility of the Jena University Hospital in strict compliance with the European Union guidelines and approved by the *Thüringer Landesamt für Verbraucherschutz*.

All biological samples from rats (tissues; primary cells) were obtained from animals that were sacrificed by cervical dislocation by trained personnel. Murine organs were obtained from mice sacrificed by cervical dislocation (ages P8 and older) and decapitation (ages P0–P4), respectively. Embryos were removed from uteri and additionally decapitated. The training status of the personnel involved was approved by the *Thüringer Landesamt für Verbraucherschutz*.

## Results

### Identification and verification of EHBP1 as a binding partner of syndapin family members

The BAR domain superfamily protein syndapin I is enriched in neurons and critically involved in neuronal morphology establishment during early and late stages of development. The molecular mechanisms syndapin I uses seem to involve complex

interactions with the plasma membrane and with further effector proteins that we are only beginning to understand (Dharmalingam et al., 2009; Schneider et al., 2014; Izadi et al., 2021). In order to unveil such molecular mechanisms, we conducted an in silico screen with a consensus for syndapin I SH3 domain interaction motifs deduced from the syndapin I binding sites identified in Cobl and Cobl-like (Schwintzer et al., 2011; Izadi et al., 2021). Running the consensus obtained from 27 species K-[RAGS]-[RKQ]-A-P-[PLAS]-P-P against sequences in UniProtKB/SwissProt, UniProtKB/TrEMBL, and the PDB database yielded hundreds of sequences including 201 of vertebrate origin. Among those, 54 and 41 sequences represented Cobl-like and Cobl, respectively, and 26 sequences identified represented EHBP1, a multidomain EHD protein-binding protein thought to be involved in membrane trafficking functions via its Rab8- and Rab10-binding C terminus containing a bMERB domain (Wang et al., 2016; Rai et al., 2016, 2020; Li et al., 2016; Fig. 1*A*,*B* and Fig. 1-1).

In line with the screening in silico, coprecipitation analyses confirmed the interaction of full-length rat EHBP1 with syndapin I as well as with the long and short variant of the more ubiquitously expressed syndapin II (Fig. 1*C*). In contrast, a mutant EHBP1 lacking the proposed syndapin binding motif (EHBP1$^{\Delta KRAP}$) was not coprecipitated (Fig. 1*C*).

Specific coimmunoprecipitations with both the N-terminal half as well as a proline-rich domain of EHBP1, which contains both EHBP1's NPF motifs as well as the KRAP motif critical for syndapin binding, demonstrated the relevance of EHBP1 interaction with all three syndapin family members in cells (Fig. 1*D–F*).

### EHBP1 is a brain-enriched, membrane-associated protein

Western blot analyses showed that EHBP1 is highly expressed in several tissues. Particularly, the testis, brain, lung, and colon showed high EHBP1 expression (Fig. 1*G*). Several tissues, such as the spleen and heart, showed two discrete bands at slightly lower molecular weights than the ∼180 kD band, which seemed to be specifically present in the brain (Fig. 1*G*). EHBP1 cloning efforts from rat brain cDNA indeed exclusively led to the longest form of EHBP1. In contrast, cloning efforts from heart cDNA solely yielded splice variants lacking aa213–247 and/or aa879–914 corresponding to rat EHBP1 isoforms X3 (Δ213–247; XP_006251628) and X4 (Δ879–914; XP_006251629) and/or X7 (Δ213–247 and Δ879–914; XP_038948016), respectively. For human EHBP1, similar splice isoforms were deduced (Fig. 1-2). The high expression of EHBP1 in the brain reflected an expression in neurons. Cultures of primary neurons showed a clear anti-EHBP1 immunosignal, whereas primary cultures of glial cells did not (Fig. 1*H*).

Subcellular fractionation experiments using rat brain material suggested that—similar to syndapin I—significant portions of EHBP1 can be found in the S2 fraction as well as in the membrane fraction (P2′). Further dissection on density gradients suggested that both EHBP1 and syndapin I to a significant extent were present in synaptosomes. Synaptosome extractions by osmotic shock demonstrated that both syndapin I and EHBP1 were abundant at isolated synaptic membranes (Fig. 1*I*).

### EHBP1 forms complexes with syndapin I in neurons

We next addressed EHBP1/syndapin I complex formation in rat brain samples. Immobilized, recombinant rat EHBP1 fusion proteins comprising the KRAP motif (EHBP1$^{267–394}$ and EHBP1$^{267–529}$) are specifically associated with endogenous syndapin I from rat brain lysates (Fig. 2*A*). Vice versa, both syndapin I full-length and the syndapin I SH3 domain specifically coprecipitated endogenous EHBP1 from rat brain lysates (Fig. 2*B*).

Furthermore, endogenous EHBP1 was specifically coimmunoprecipitated with endogenous syndapin I from rat brain lysates using affinity-purified polyclonal anti-syndapin I antibodies (Fig. 2*C*). The successful coimmunoprecipitation of the two endogenous proteins from rat brain lysates strongly suggested an in vivo-relevance of the EHBP1 interaction with syndapin I in the brain.

In order to firmly demonstrate that the interaction of EHBP1 and syndapin I can indeed be observed in intact hippocampal rat neurons, we expressed a syndapin I variant (Mito-mCherry-SdpI) that was effectively targeted to mitochondrial membranes, as demonstrated by colocalization with cytochrome *c* as mitochondrial marker (Fig. 2*D*). Strikingly, in neurons expressing mitochondrially targeted syndapin I, EHBP1 showed an alteration of subcellular distribution and accumulated at the syndapin I-decorated mitochondria (Fig. 2*D*). In control experiments with a mitochondrially targeted syndapin I mutant lacking the EHBP1-binding SH3 domain (Mito-mCherry-SdpI$^{\Delta SH3}$), EHBP1 did not show an alteration of its subcellular distribution (Fig. 2*E*). This proved the specificity and the SH3 domain dependence of the visualized EHBP1 complex formation with syndapin I in primary rat hippocampal neurons.

### EHBP1 gain of function promotes the formation of the dendritic arbor in developing neurons, and this function is dependent on its syndapin I binding interface

The functions of mammalian EHBP1 in neurons were unknown. Interestingly, EHBP1 expression was already readily detectable at the embryonic stages E16 and E18 and did not increase further postnatally, that is, did not strongly correlate with synapse formation, function, and/or plasticity (Fig. 3*A*). We therefore in detail analyzed EHBP1's putative role in early neuronal development. Developing primary rat hippocampal neurons at DIV6 showed EHBP1 immunoreactivity in perinuclear areas, the cytoplams as well as in F-actin-rich areas of the cell cortex, such as lamellipodial areas and neuritic growth cones (Fig. 3*B*). The validity of the anti-EHBP1 immunostaining in primary rat hippocampal neurons was demonstrated by RNAi experiments showing a severe reduction of anti-EHBP1 immunosignals in neurons transfected with EHBP1 RNAi but not in neurons transfected with scrambled RNAi when compared to neighboring, untransfected cells (Fig. 3*C*,*D*).

Imaris software-based 3D reconstructions of neuronal morphologies at DIV6 showed a surplus of dendritic branching points and dendritic terminal points of GFP-EHBP1-expressing neurons when compared to GFP-expressing control neurons (Fig. 3*E–H*). The summarized dendritic length was only modestly and not statistically significantly increased (Fig. 3*H*). Sholl analyses demonstrated an increased complexity of the dendritic arbor of EHBP1-overexpressing neurons and thereby clearly confirmed the discovered EHBP1 gain-of-function phenotype (Fig. 3*I*).

The Sholl analyses showed no statistically significant increase in Sholl intersections at a 10 µm distance from the cell center (Fig. 3*I*), that is, suggested that the EHBP1 gain-of-function phenotype mainly reflected an increase in dendritic branches in the dendritic arbor and not an increase of primary dendrites emanating from the cell body. Branch depth analyses demonstrated that EHBP1 gain-of-function caused significant effects at branch

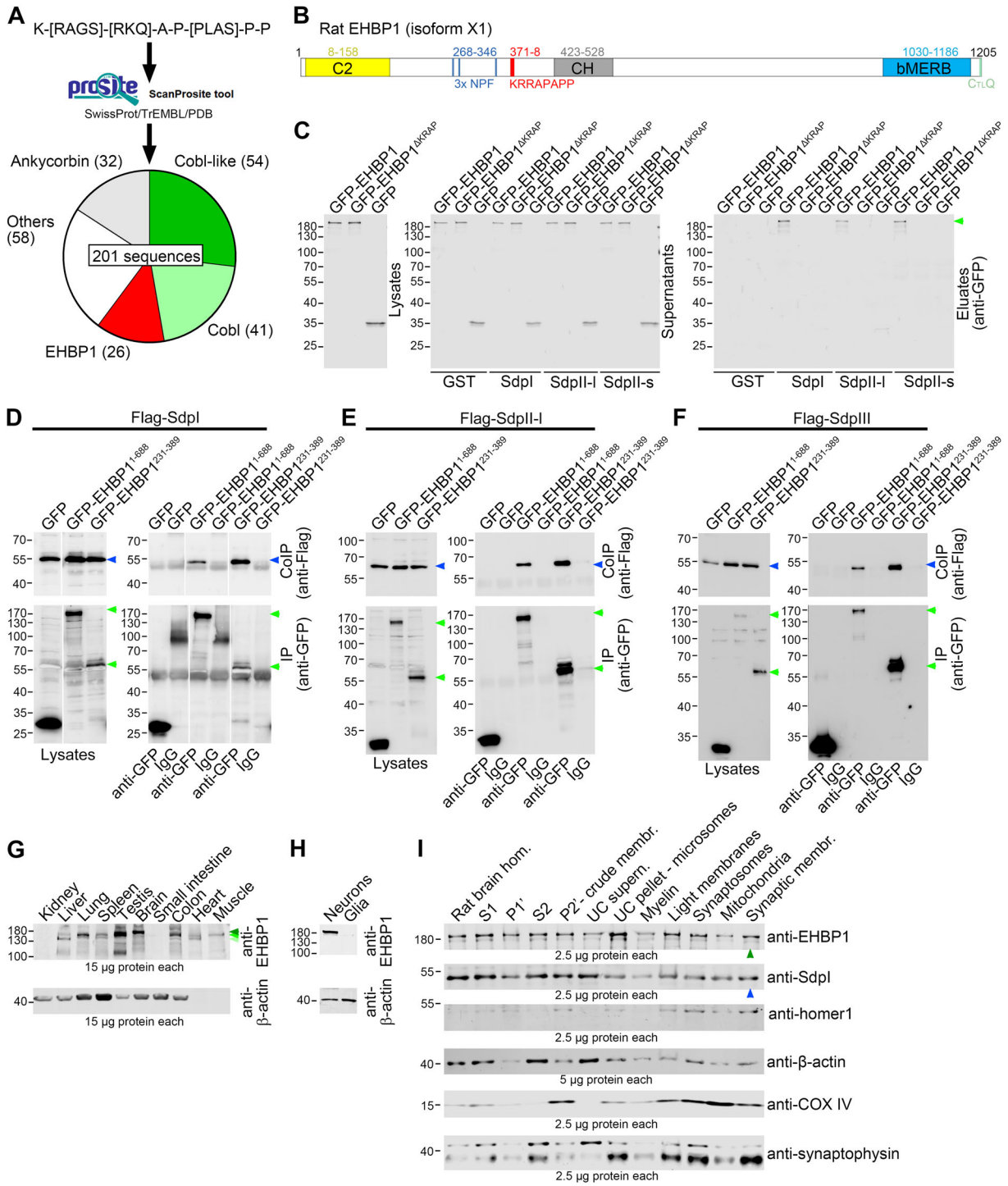


**Figure 1.** Identification and verification of EHBP1 as a binding partner of syndapin family members. ***A***, In silico searches with the indicated syndapin I SH3 domain binding consensus sequence (deduced from the identified binding sites in Cobl and Cobl-like) yielded a total of 201 sequences from vertebrates. The portion of EHBP1 sequences (26 sequences from 16 species) is shown in red. ***B***, Schematic representation of rat EHBP1 (isoform X1; XP_017454733) and its amino acid motifs (sequences below the scheme) and domains (labeled inside the scheme; C2, calcium-binding domain 2; CH, calponin homology; bMERB, bivalent Mical/EHBP Rab binding). For alignment of human, mouse, and rat EHBP1, see Fig. 1-1. ***C***, Coprecipitation of GFP-tagged rat EHBP1 (XP_017454733; green arrowhead) but not EHBP1$^{\Delta KRAP}$ with immobilized GST-syndapin I (SdpI), as well as the long (SdpII-l) and short (SdpII-s) splice isoforms of syndapin II, respectively. ***D–F***, Coimmunoprecipitations demonstrating a specific association of GFP-EHBP1$^{1-688}$ (aa1–688 of the human EHBP1 isoform 2; NP_001136086) and also of GFP-EHBP1$^{231-389}$ (NPF and KRAP motif region of human EHBP1 isoform 2; corresponding to aa266–424 in the longest human EHBP1 variant, i.e., isoform 1; NP_056067; see Fig. 1-2 for schematic overview) with Flag-tagged syndapin I (***D***), syndapin II-l splice variant (***E***), and syndapin III (***F***). Positions of syndapins (CoIPs) are marked by blue arrowheads, and positions of GFP-EHBP1$^{1-688}$ and GFP-EHBP1$^{231-389}$ (IPs) are marked by green arrowheads. White lines (in ***D***) represent lanes omitted from the blot image. ***G***, Anti-EHBP1 immunoblotting of lysates from different murine organs. For each lane, 15 µg protein was loaded. Arrowheads mark the size of EHBP1 (dark green) and smaller splice variants thereof (two lighter greens). Note that in the brain, exclusively the longest EHBP1 form seems to be expressed. ***H***, Anti-EHBP1 immunoblotting analyses of lysates of neuronal cultures and glial cultures showing a neuron-specific expression of EHBP1. ***I***, Immunoblotting analyses of subcellular fractionations of rat brain material. The anti-EHBP1 and anti-syndapin I immunoblotting analyses of the brain fractionation experiments are complemented with data for additional marker proteins [COX IV, mitochondria; synaptophysin, (pre)synaptic plasma membrane-associated]. Note that EHBP1 and syndapin I as well as homer1 (PSD component) and synaptophysin are readily detectable in the synaptic membrane fraction generated from density gradient-purified synaptosomes extracted by osmotic shock (arrowheads).

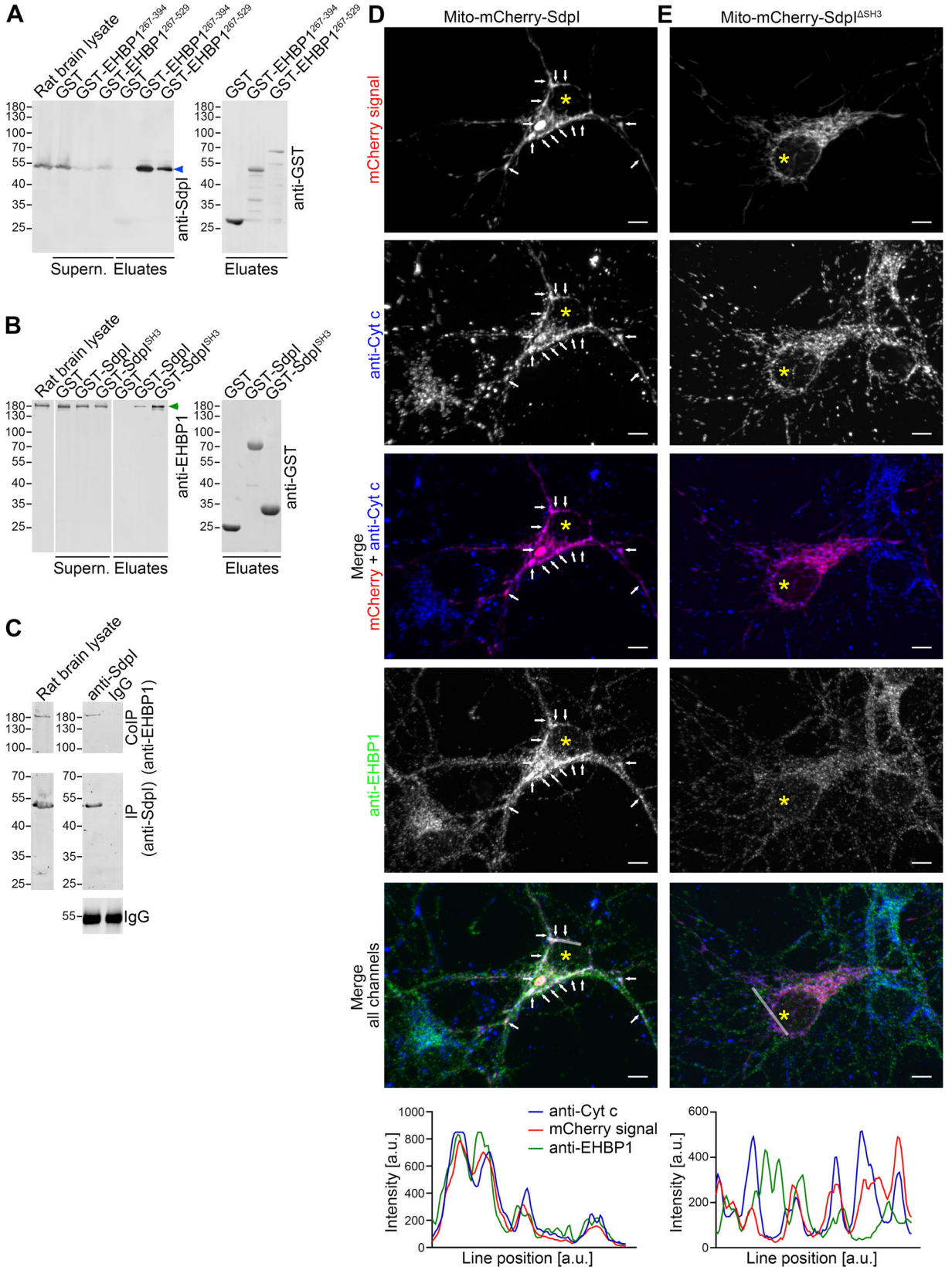


**Figure 2.** Continued.

depth levels 2 and 3 ($p < 0.05$ and $p < 0.001$, respectively; Fig. 3*J*). In contrast, we did not observe any significant increase in branch depth level 1 reflecting primary dendrites when GFP-EHBP1-overexpressing neurons were compared to GFP-expressing control cells (Fig. 3*J*).

Strikingly, all EHBP1-mediated changes in dendritic arborization were critically dependent on the identified syndapin I binding interface, as EHBP1$^{\Delta KRAP}$ completely failed to show a similar phenotype (Fig. 3*E–J*). Importantly, this mutation did neither impair protein stability nor the established interaction of EHBP1 with EHD1 (Fig. 3*K*). Upon expression of the EHBP1$^{\Delta KRAP}$ mutant, all dendritic arborization parameters differed in a highly statistically significant manner from those determined for EHBP1-overexpressing neurons. Comparisons to GFP control cells demonstrated that, despite the deletion of only very few amino acids (ΔKRRAPAPP; Δaa371–378 of rat EHBP1), the syndapin I binding-deficient EHBP1$^{\Delta KRAP}$ mutant failed to elicit any effects on dendritic branching (Fig. 3*E–J*).

### EHBP1's functions in dendritic arbor formation rely on syndapin I

Further supporting an important function of EHBP1 in promoting dendritic arborization, the EHBP1 gain-of-function phenotypes were likewise observed when GFP-EHBP1 and scrambled RNAi-encoding plasmids were coexpressed. Additionally, the moderate increase in total dendritic tree length was statistically significant in this paradigm (Fig. 4*A–E*). These results allowed for addressing a putative syndapin I requirement in EHBP1-mediated dendritic arbor formation. Importantly, RNAi-mediated knockdown of syndapin I expression completely disrupted EHBP1-mediated dendritic arborization, as all quantitative dendritic parameters of EHBP1 and syndapin I RNAi-expressing neurons were strongly diminished to values even below control levels. In fact, EHBP1 and syndapin I RNAi-expressing neurons displayed values of all parameters that were similar or even slightly below those determined for GFP and syndapin I RNAi-expressing neurons (Fig. 4*A–E*). Therefore, the values clearly represented a full suppression of the EHBP1 gain-of-function phenotype by syndapin I deficiency.

Taken together, our examinations unveiled that EHBP1 overexpression promotes dendritic arborization and that this function of EHBP1 is strictly dependent on its syndapin I binding interface as well as on the presence of syndapin I in the developing neurons.

### EHBP1 transiently occurs at dendritic sites forming new branches

Analyses of the temporal and spatial dynamics of EHBP1 in relation to dendritic branch formation processes using 3D time-lapse imaging of developing primary hippocampal neurons expressing GFP-EHBP1 revealed that EHBP1 was present at dendritic branch sites prior to dendritic branch induction (Fig. 5*A*).

Quantitative assessments showed that EHBP1 accumulated at such sites when compared to non-branching areas of the same dendrite (about +60%). The EHBP1 accumulation thereby was about 3 times as high as that of mCherry used as unspecific protein control (Fig. 5*B*).

Frequently, GFP-EHBP1 did not just accumulate at the branch initiation site but also inside the forming dendritic protrusion (Fig. 5*A*, arrowhead).

In general, the dynamic behavior of GFP-EHBP1 in developing neurons was in line with the hypothesis that EHBP1 may play some role in dendritic arbor formation.

### EHBP1 deficiency leads to impaired dendritic arbor formation

In order to be able to address whether EHBP1 is not only able to promote dendritic arborization in developing neurons but may also be critical for this biological process, we next established EHBP1 RNAi. Quantitative, fluorescence-based Western blot analyses demonstrated that even a CMV promotor-driven expression of EHBP1 by a heterologous expression system was successfully and very strongly suppressed by accompanying EHBP1 RNAi (Fig. 6*A*,*B*).

Rat primary hippocampal neurons transfected with EHBP1 RNAi were marked by impaired dendritic arborization when compared to neurons expressing scrambled RNAi (Fig. 6*C*). Quantitative analyses of the anti-MAP2-stained dendritic arbor using 3D reconstructions by Imaris revealed that a lack of EHBP1 led to significantly reduced numbers of dendritic branching points (Fig. 6*D*), to fewer terminal points (Fig. 6*E*), and also to a reduced total length of the dendritic tree (Fig. 6*F*). With ∼30% fewer dendritic branches and ∼20% fewer dendritic terminal points at the end of the development from DIV4 (transfection) to DIV6 (fixation), the EHBP1 loss-of-function phenotype was pronounced (Fig. 6*D*,*E*). Sholl analyses also clearly showed the impaired dendritic arbor development and highlighted that, while initial dendrite formation from the cell body seemed to be unaffected, EHBP1 loss-of-function effects occurred inside the entire dendritic arbor (Fig. 6*G*).

Dendritic branch depth analyses demonstrated no branch depth level 1 alterations in neurons expressing EHBP1 RNAi in comparison to scrambled RNAi. In contrast, in particular, the higher branch depth levels (2–4) showed EHBP1 RNAi-mediated decreases (Fig. 6*H*). These data clearly demonstrate that, whereas the number of primary dendrites (branch depth level 1) was unchanged upon EHBP1 loss-of-function, EHBP1 plays a critical role in dendritic branching.

The identified EHBP1 loss-of-function phenotypes (Fig. 6) were opposite to the effects of EHBP1 gain-of-function

←

**Figure 2.** EHBP1 forms complexes with syndapin I in neurons. ***A***, Coprecipitation of endogenous syndapin I (marked by a blue arrowhead) from rat brain lysates using two different GST fusion proteins of rat EHBP1 (GST-EHBP1$^{267-394}$ and GST-EHBP1$^{267-529}$). ***B***, Coprecipitation of endogenous EHBP1 (marked by green arrowhead) from rat brain lysates by immobilized GST-SdpI as well as with GST-SdpI$^{SH3}$. White lines (in ***B***) represent lanes omitted from the blot. ***C***, Coimmunoprecipitation of endogenous EHBP1 and syndapin I from rat brain. Affinity-purified rabbit anti-syndapin I antibodies specifically immunoprecipitated endogenous syndapin I and coimmunoprecipitated endogenous EHBP1 from rat brain lysates, as detected by affinity-purified anti-syndapin I antibodies raised in guinea pig (IP, middle panel) and anti-EHBP1 antibodies (CoIP, upper panel). Non-immune IgGs served as negative control. Lower panels show the use of equal amounts of antibodies. ***D***,***E***, Merged images of visualizations of EHBP1/syndapin I complex formations in primary hippocampal neurons at specific subcellular membranes (mitochondria) decorated with syndapin I (Mito-mCherry-SdpI; ***D***) and with Mito-mCherry-SdpI$^{\Delta SH3}$ (***E***), respectively. Transfected neurons are marked with yellow asterisks. Colocalizations of Mito-mCherry-SdpI (***D***; red in merges) and Mito-mCherry-SdpI$^{\Delta SH3}$ (***E***; red in merges) with immunostainings for the mitochondrial marker cytochrome *c* (Cyt c; blue in merges) prove the successful targeting of both syndapin I tools to mitochondria (merge mCherry + anti-Cyt c signals; colocalizations appear as magenta). Note that Mito-mCherry-SdpI-expressing neurons (***D***) show recruitment and accumulation of endogenous EHBP1 (green in merges) at mitochondria (***D***), whereas Mito-mCherry-SdpI$^{\Delta SH3}$-expressing neurons (***E***) do not. Colocalizations of all three channels, that is, of mCherry, anti-Cyt c, and anti-EHBP1 signals, appear white in the merged images (see the lower image in ***D***; white arrows mark examples). Bars, 5 µm. Colocalizations were additionally addressed by line scans (lower panels) along the half-transparent lines depicted in the merges. For an EHBP1 RNAi-based validation of the anti-EHBP1 immunostaining in hippocampal neurons see Fig. 3*C*.

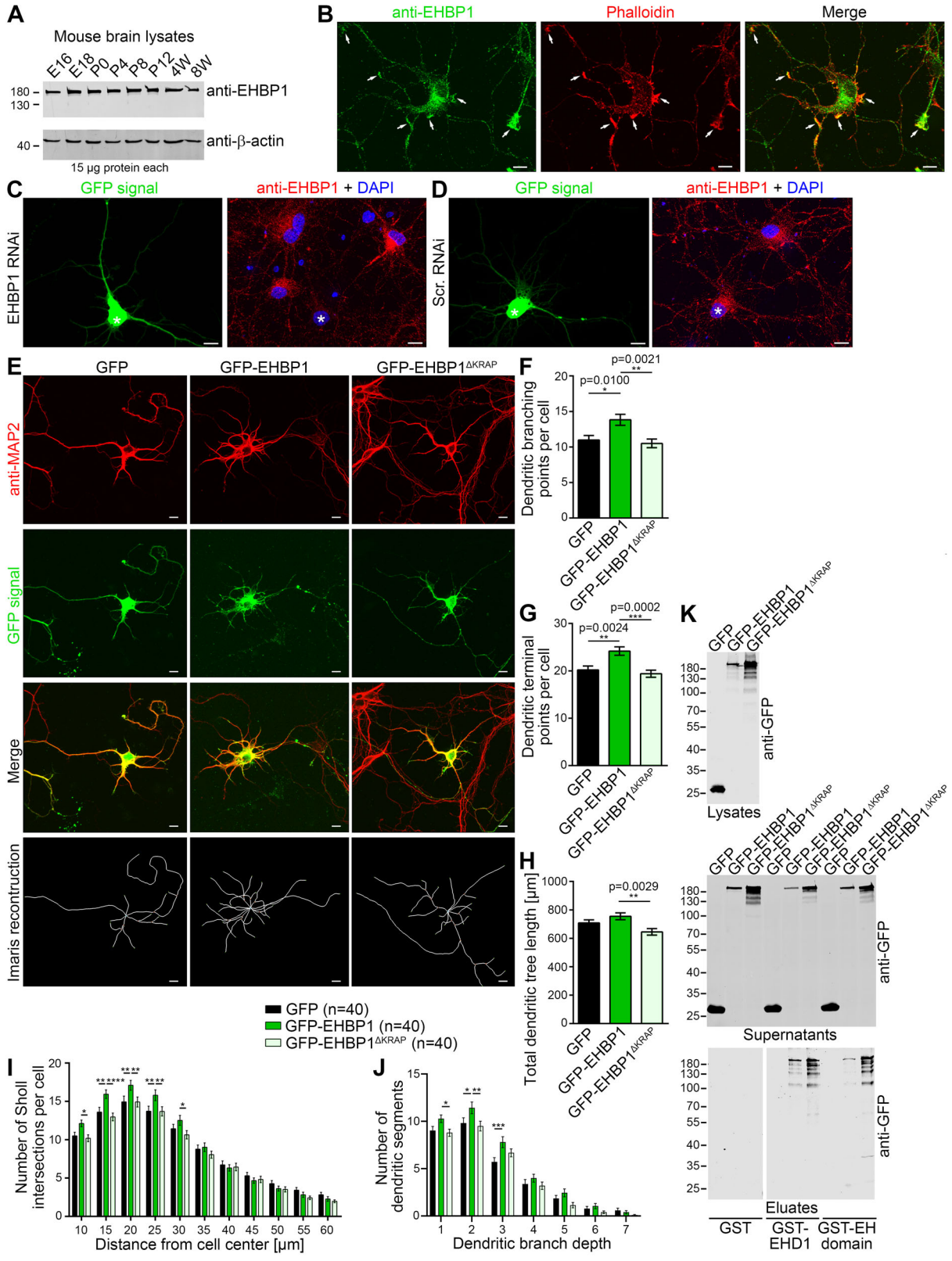


**Figure 3.** Continued.

phenotypes (Figs. 3, 4). Both types of functional analyses thus were in line and pointed out that EHBP1 plays a role in the dendritic arborization of developing neurons.

### The EHBP1 loss-of-function phenotype in dendritic branching can be rescued by reexpression of EHBP1 but is not effectively rescued by an EHBP1 mutant unable to associate with syndapin I

Rescue experiments proved the specificity of the identified EHBP1 loss-of-function phenotypes. Resupplying EHBP1-deficient neurons with RNAi-insensitive EHBP1 (GFP-EHBP1*) led to a rescue of the EHBP1 loss-of-function phenotypes in dendritic branch points, terminal points, and total dendritic length, as the values of all of these parameters were statistically indistinguishable from control levels (scrambled RNAi; Fig. 7*A–D*). The fact that for all dendritic parameters also a strong statistical difference from the EHBP1 RNAi data was obtained proved the successful rescue by GFP-EHBP1* and thereby clearly demonstrated the specificity of the EHBP1 RNAi phenotypes in dendritic branching (Fig. 7*A–D*).

Interestingly, in sharp contrast, reexpression of the RNAi-insensitive but syndapin binding-incompetent mutant GFP-EHBP1*$^{\Delta KRAP}$ failed to effectively rescue the EHBP1 RNAi-mediated reduction of both dendritic branching points and terminal points. Both of these dendritic branching parameters remained statistically indistinguishable from those of EHBP1 RNAi neurons (Fig. 7*B*,*C*).

Merely in the total dendritic tree length, GFP-EHBP1*$^{\Delta KRAP}$ was able to rescue the EHBP1 deficiency effects (Fig. 7*D*). Sholl analyses uncovered the reasons underlying these observations. In the periphery (Sholl intersections ≥30 µm), the rescue by GFP-EHBP1* was partial, and GFP-EHBP1*$^{\Delta KRAP}$ had relatively equal effects. However, in the proximal dendritic arbor (e.g., at Sholl intersections 15 and 20 µm), the rescue by GFP-EHBP1* reexpression was about complete, but EHBP1*$^{\Delta KRAP}$ completely failed to restore any of these EHBP1 functions (Fig. 7*E*).

Taken together, the fact that EHBP1-mediated dendritic arbor formation completely relies on syndapin I (Fig. 4) and on the syndapin I-binding KRAP motif of EHBP1 (Fig. 3) was mirrored by EHBP1 loss-of-function analyses (Fig. 7). These studies revealed that, in proximal areas, the syndapin I binding site was absolutely critical for proper dendritic arbor formation.

### Syndapin I-mediated dendritic arbor formation requires EHBP1

Syndapin I promotes neuromorphogenesis (Dharmalingam et al., 2009) by cooperating with additional factors that are only emerging. While syndapin I deficiency led to reduced dendritic arborization and schizophrenia-like symptoms (Koch et al., 2020), an excess of syndapin I in developing neurons resulted in an increase in dendritic branching, in the number of terminal points and in the total length of the dendritic tree. Strikingly, all of these syndapin I gain-of-function phenotypes were suppressed by coexpression of EHBP1 RNAi (Fig. 8*A–E*). All dendritic parameters of syndapin I and EHBP1 RNAi-cotransfected neurons were statistically significantly different from those of neurons expressing syndapin I alone. Furthermore, the suppression of syndapin I-mediated dendritic arborization by EHBP1 RNAi was so severe that the dendritic arborization parameters of SdpI+EHBP1 RNAi-transfected neurons appeared to be below control levels (Scr. RNAi). The data for dendritic branching, terminal points, and total dendritic length were indistinguishable from the diminished values determined for EHBP1-deficient neurons (Fig. 8*B–E*).

This suggested that these effects do not merely represent putative parallel additive effects but reflect a full repression of the syndapin I phenotype by EHBP1 deficiency (Fig. 8*A–E*). This effective suppression of syndapin I function by EHBP1 was detected in all areas of the dendritic tree marked by syndapin I-driven increases in dendritic complexity (Fig. 8*E*).

### EHBP1 functions in dendritic arborization do not require its C-terminal bMERB domain but require its membrane-binding C2 and actin-binding CH domains

Our studies revealed that EHBP1 works together with syndapin I in dendritic arbor formation. EHBP1, however, is a multidomain protein. It thus was important to address which domains and molecular mechanisms besides the thus far studied physical and functional coupling to syndapin I may also be involved in the identified function of EHBP1 in the mammalian neuronal context. We therefore next dissected EHBP1 functions further by conducting rescue experiments with additional EHBP1 mutants. Besides the ΔKRAP mutant, these included mutants lacking the bMERB domain, the CH domain, and the C2 domain, respectively (Fig. 9). Interestingly, although all of the tested mutants were still able to mediate the established interaction of EHBP1 with EHD1 (Fig. 9), two of these additional mutants failed to support dendritic branching (Fig. 10*A–E*). Deletion of EHBP1's actin-binding CH domain as well as deletion of EHBP1's N-terminal membrane-binding C2 domain both completely failed to rescue the EHBP1 loss-of-function phenotypes in dendritic branching. The dendritic branching points, the terminal points, and the total dendritic tree length of neurons

←

**Figure 3.** EHBP1 gain-of-function promotes the formation of the dendritic arbor in developing neurons. ***A***, Immunoblotting analyses of EHBP1 expression in brain lysates generated from mice of different developmental stages ranging from the embryonal stages E16 and E18, over the postnatal days 0–12 (P0–P12) to the juvenile and adolescent stages of 4 and 8 weeks, respectively. Anti-β-actin staining is shown for comparison. ***B***, Maximum intensity projections (MIPs) of Apotome image stacks of primary rat hippocampal neurons at DIV6 that were immunostained for endogenous EHBP1 and stained for F-actin (visualized by phalloidin). Arrows highlight examples of EHBP1 colocalization with enrichments of F-actin at the cell cortex and in growth cones. ***C***,***D***, EHBP1 RNAi-based validation of the specificity of the anti-EHBP1 immunostaining in neurons transfected at DIV4 and immunostained with anti-EHBP1 antibodies at DIV6. Note that the anti-EHBP1 immunoreactivity is strongly diminished in EHBP1 RNAi-transfected cells (GFP-reported) when compared to neighboring untransfected cells (***C***) or compared to scrambled RNAi-transfected neurons (GFP-reported; ***D***). Transfected neurons are marked with white asterisks. Blue, DAPI. ***E***, Representative MIPs of primary rat hippocampal neurons that had been transfected at DIV4 with either GFP, GFP-EHBP1, and GFP-EHBP1$^{\Delta KRAP}$, respectively, and were fixed 40 h later. Imaris reconstructions of neuronal morphology are based on immunostainings of the dendritic marker MAP2. Bars, 10 µm (***B–E***). ***F–J***, Quantitative determinations of dendritic branching points (***F***), dendritic terminal points (***G***), total dendritic tree length (***H***), Sholl analyses (***I***), and dendritic branch depth analyses (***J***). Data, mean ± SEM. GFP, $n = 40$; GFP-EHBP1, $n = 40$; GFP-EHBP1$^{\Delta KRAP}$, $n = 40$ neurons (from 4 independent coverslips and 2 independent neuronal preparations). One-way ANOVA with Tukey posttest (***F–H***) and two-way ANOVA with Sidak posttest for Sholl analysis (***I***) and dendritic branch depth analyses (***J***). *$p < 0.05$; **$p < 0.01$; ***$p < 0.001$; ****$p < 0.0001$ (for ***F–H***, exact $p$ values are provided directly in the figure panels; note that $p$ values <0.0001 are not reported by Prism 6 software). ***K***, Immunoblotting analyses of coprecipitation experiments with GFP, GFP-EHBP1, and GFP-EHBP1$^{\Delta KRAP}$ and immobilized, recombinant GST, GST-EHD1, and the GST-EH domain of EHD1. Note that in contrast to its disrupted syndapin binding caused by the deletion of the KRAP motif (Fig. 1), GFP-EHBP1$^{\Delta KRAP}$ readily associates with EHD1 and the EH domain of EHD1 (see eluates).

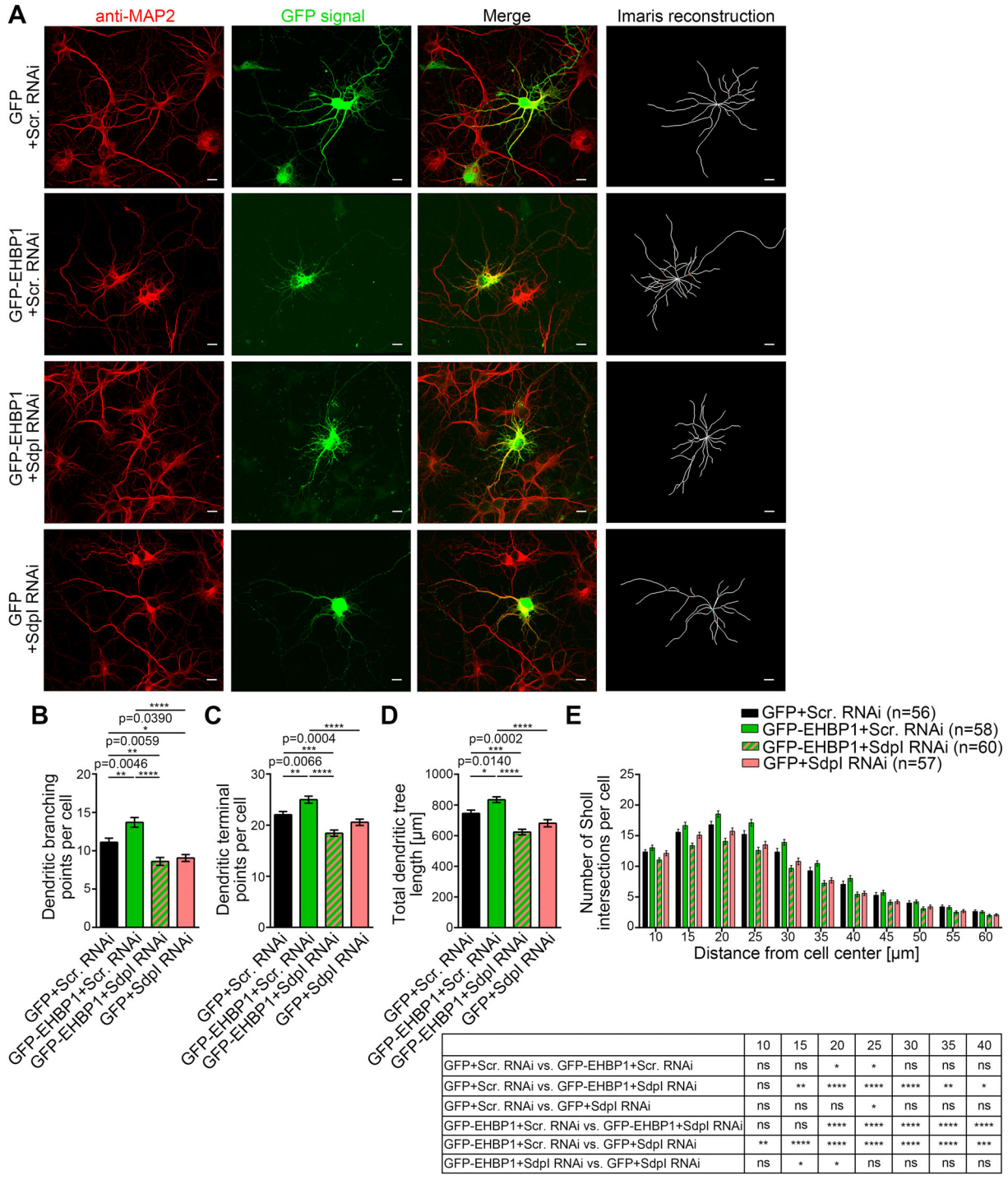


| | 10 | 15 | 20 | 25 | 30 | 35 | 40 |
|---|---|---|---|---|---|---|---|
| GFP+Scr. RNAi vs. GFP-EHBP1+Scr. RNAi | ns | ns | * | * | ns | ns | ns |
| GFP+Scr. RNAi vs. GFP-EHBP1+SdpI RNAi | ns | ** | **** | **** | **** | ** | * |
| GFP+Scr. RNAi vs. GFP+SdpI RNAi | ns | ns | ns | * | ns | ns | ns |
| GFP-EHBP1+Scr. RNAi vs. GFP-EHBP1+SdpI RNAi | ns | ns | **** | **** | **** | **** | **** |
| GFP-EHBP1+Scr. RNAi vs. GFP+SdpI RNAi | ** | **** | **** | **** | **** | **** | *** |
| GFP-EHBP1+SdpI RNAi vs. GFP+SdpI RNAi | ns | * | * | ns | ns | ns | ns |

**Figure 4.** EHBP1's functions in dendritic arbor formation critically rely on syndapin I. ***A***, MIPs of anti-MAP2 labeled neurons that had been transfected with combinations of GFP and scrambled RNAi (GFP + Scr. RNAi), GFP-EHBP1 and scrambled RNAi (GFP-EHBP1 + Scr. RNAi), GFP-EHBP1 and syndapin I RNAi (GFP-EHBP1 + SdpI RNAi), as well as with GFP and syndapin I RNAi (GFP + SdpI RNAi) at DIV4 and fixed 2 d later and 3D reconstructions of neuronal morphology by Imaris software. The RNAi plasmids were reported by mCherry coexpression. Scale bars, 10 µm. ***B–E***, Quantitative determinations of the key dendritic arborization parameters dendritic branching points (***B***), dendritic terminal points (***C***), total length of the dendritic tree (***D***), and Sholl intersections (***E***) promoted by EHBP1 and their dependence on syndapin I. Data, mean ± SEM. GFP + Scr. RNAi, $n = 56$; GFP-EHBP1 + Scr. RNAi, $n = 58$; GFP-EHBP1 + SdpI RNAi, $n = 60$; GFP + SdpI RNAi, $n = 57$ neurons of 6 independent coverslips and 3 independent neuronal preparations. One-way ANOVA with Tukey's posttest (***B–D***) and two-way ANOVA with Sidak posttest for Sholl analysis (***E***). *p < 0.05; **$p < 0.01$; ***$p < 0.001$; ****$p < 0.0001$ (exact $p$ values are provided directly in the figure panels ***B–D***; note that $p$ values <0.0001 are not reported by Prism 6 software).

reexpressing these two mutants were indistinguishable from the values determined for EHBP1-deficient neurons (Fig. 10*A–E*).

Thus, besides syndapin I and the syndapin I-binding KRAP motif of EHBP1, EHBP1's $Ca^{2+}$-regulated and membrane-binding C2 domain and EHBP1's CH domain mediating actin cytoskeletal interactions are critical for EHBP1 functions in dendritic arborization.

In contrast to the observed critical functions of EHBP1's CH and C2 domains, expression of an RNAi-resistant EHBP1 mutant lacking the C-terminal part including the Rab GTPase-

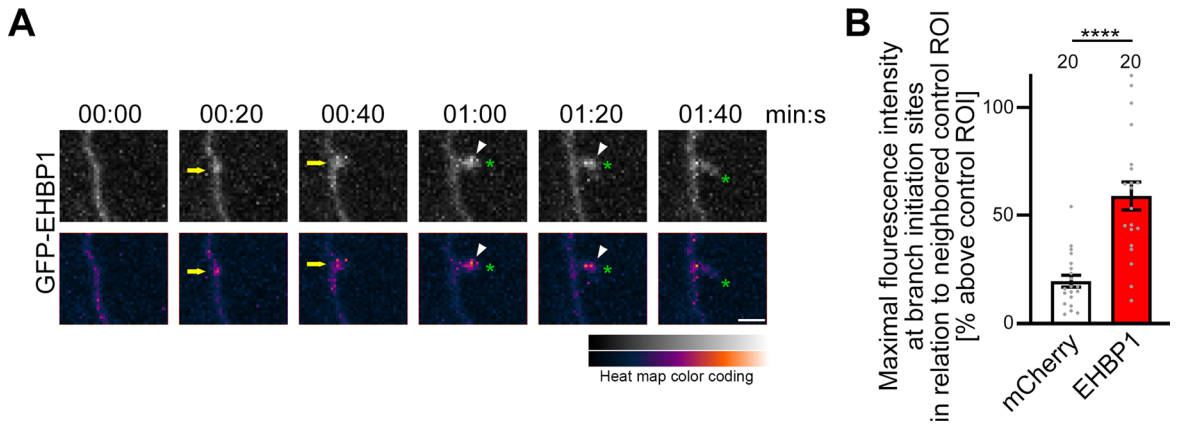


**Figure 5.** EHBP1 transiently accumulates at nascent dendritic branch sites and also occurs in forming dendritic protrusions. ***A***, Image gallery (MIPs) of six individual frames of 3D time-lapse analyses of GFP-EHBP1 at nascent dendritic branch sites of developing hippocampal neurons transfected at DIV6 and imaged 14–17 h thereafter using a spinning disc microscope with a frame rate of 10 s per image stack. Shown are black and white representations of fluorescence (upper panels) and a false-color (*gem*) heat map representation of the spatiotemporal behavior of GFP-EHBP1 during dendritic branch initiation (lower panels; for heat map color coding, see legend). Green asterisks track the tip position of the growing protrusion. Arrows mark EHBP1's accumulation at the nascent dendritic branch site and white arrowheads mark the EHBP1 accumulation inside of a newly formed dendritic branch during the first seconds of its outgrowth (see 1:00 and 1:20 min:s frames). Bar, 2 µm. ***B***, Quantitative determinations of maximal fluorescence intensities of GFP-EHBP1 at nascent dendritic branch sites in relation to signals inside of control ROIs at non-branching dendritic sites. Corresponding determinations for mCherry are shown as control. Data, mean ± SEM and individual data points. mCherry and GFP-EHBP1, $n = 20$ determinations in 10 (mCherry) and in 5 (GFP-EHBP1) transfected neurons, respectively (each obtained from at least 2 independent preparations of primary neuronal cultures). Mann–Whitney *U* test. ****$p < 0.0001$ (note that $p$ values <0.0001 are not reported by Prism 6 software).

binding bMERB domain very effectively rescued the EHBP1 RNAi-impaired dendritic arbor development (Fig. 10*A–E*). This very powerful rescue was obtained for all dendritic parameters. Dendritic branching points, dendritic terminal points, and the total dendritic length as well as Sholl analysis data of neurons coexpressing GFP-EHBP1*$^{\Delta bMERB}$ with EHBP1 RNAi all were indistinguishable from those of control cells (neurons transfected with GFP-reported scrambled RNAi; Fig. 10*A–E*).

These experiments unraveled that the bMERB domain and C-terminal parts of EHBP1 are dispensable for EHBP1's functions in dendritic development, while all other domains and motifs of EHBP1 examined were absolutely critical for EHBP1 functions in the dendritic arbor formation process during neuronal development.

### EHBP1's accumulation at dendritic branch initiation sites coincides with that of syndapin I and with actin cytoskeletal structures being formed at nascent branch sites

In line with their importance in dendritic branching, EHBP1 and syndapin I colocalized at a variety of rather punctuate sites along the dendrites of developing neurons. In some cases, additional enrichments and colocalizations were observed at sites protruding from the mother dendrite (Fig. 11*A*).

Addressing whether these sites of colocalization of syndapin I and EHBP1 relate to nascent dendritic branch sites and to newly formed dendritic branches, respectively, required 3D time-lapse studies. Quantitative analyses of fluorescence intensities showed that EHBP1 accumulated at dendritic branch sites prior to dendritic branch induction in the same order of magnitude as its binding partner syndapin I (Fig. 11*B*).

3D time-lapse analyses of double-transfected primary neurons undergoing dendritic arbor development revealed that GFP-EHBP1 accumulations occurred at the same spatially confined spots (usually 0.3–1 µm in diameter) and with a similar temporal profile at the same nascent dendritic branch sites as syndapin I (Fig. 11*C*). Interestingly, the spatially very precise cooccurrence of EHBP1 and syndapin I was not limited to nascent branch induction sites but also occurred briefly and transiently inside of recently formed dendritic protrusions (Fig. 11*C*, white arrowheads, frame 1:40 min:s). Thus, EHBP1 became enriched at the same dendritic sites, which also exhibited an accumulation of EHBP1's binding partner syndapin I prior to morphologically obvious dendritic branch formation (Fig. 11*C*).

We hypothesized that the coordinated action of syndapin I and EHBP1 may include cytoskeletal contributions to dendritic branch formation. This hypothesis was supported by interactions of syndapin I with actin cytoskeletal effectors (Qualmann et al., 1999; Schwintzer et al., 2011) and was further substantiated by our observation that EHBP1's F-actin-binding CH domain was critical for EHBP1 functions in dendritic branch induction (Fig. 10). 3D time-lapse imaging of double-transfected developing neurons indeed showed that both F-actin and the syndapin I-binding actin nucleator Cobl, which would be able to promote F-actin formation at dendritic branch sites (Hou et al., 2015; Izadi et al., 2021), accumulated at nascent dendritic branch sites to about the same extent as EHBP1 and syndapin I did (Fig. 11*B*). F-actin's maximal fluorescence intensities hereby spatiotemporally coincided with those of EHBP1 at dendritic branch sides prior to branch induction (Fig. 11*D*). F-actin hereby had some tendency towards occurring at the same sites with maximal intensity about 10 s later than EHBP1 and syndapin I (Fig. 11*D*,*E*).

The syndapin I-binding actin nucleator Cobl (Schwintzer et al., 2011) also showed a temporal profile similar to those of EHBP1 and syndapin I (Fig. 11*E*) suggesting that all three components are targeted to and accumulate at the dendritic branch induction sites and help to organize and trigger local F-actin formation and subsequent branch induction.

### EHBP1 functions in dendritic arborization critically rely on the syndapin I binding partner Cobl but not on N-WASP

Besides the syndapin I interaction, our dissections of the domain requirements of mammalian EHBP1 functions in dendritic arborization suggested additional critical involvements of EHBP1 interactions with the actin cytoskeleton in dendritic branching (Fig. 10). Coaccumulations of EHBP1 with F-actin

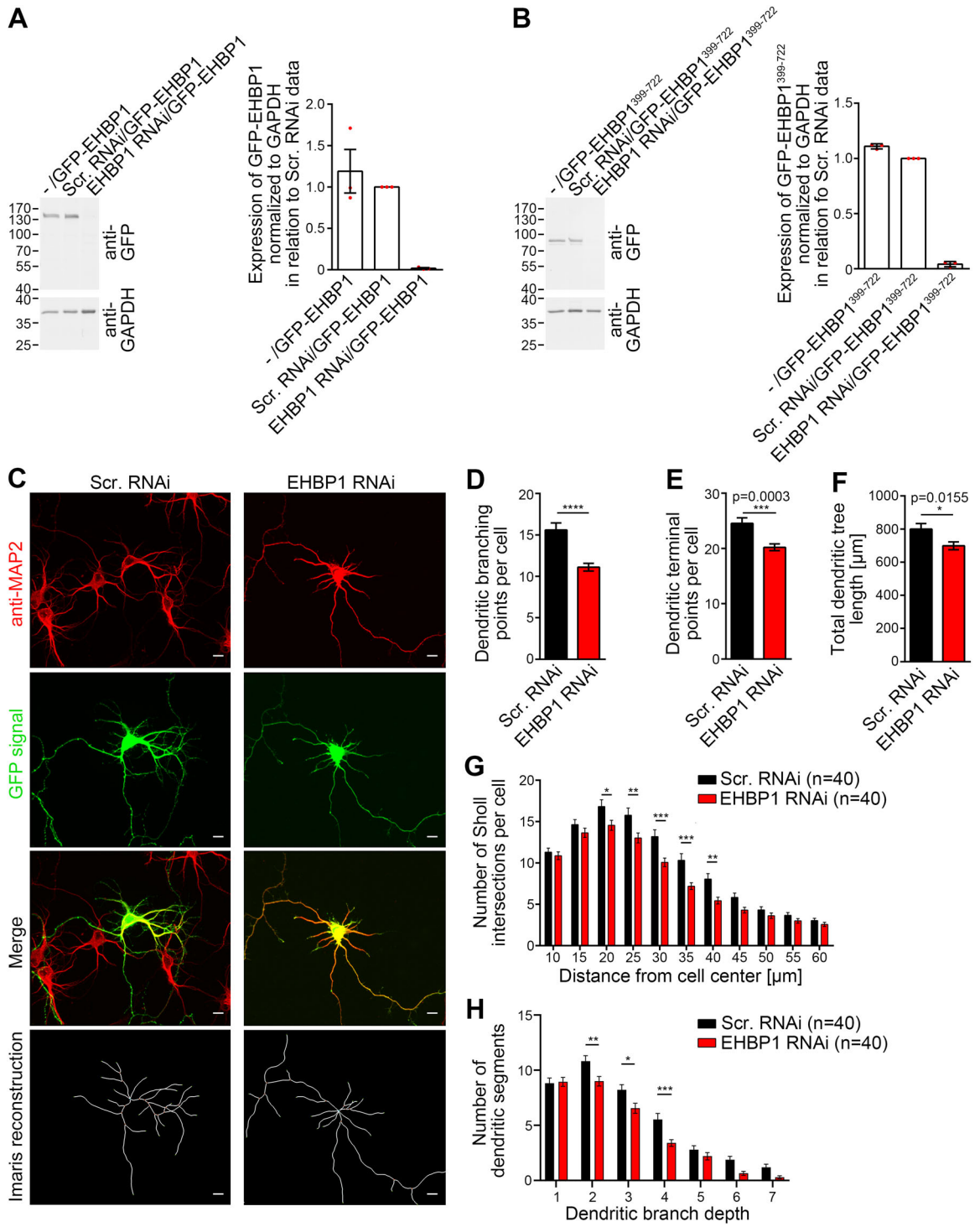


**Figure 6.** EHBP1 deficiency leads to impaired dendritic arbor formation. ***A***,***B***, Representative immunoblotting data of EHBP1 RNAi-mediated knockdown of GFP-EHBP1 (***A***) and of GFP-EHBP1$^{399–722}$ (***B***), respectively, and quantitative determinations thereof (fluorescence measurements using a LI-COR Odyssey System). GFP-EHBP1 (***A***) and GFP-EHBP1$^{399–722}$ (***B***) were expressed in HEK293 cells by pRNAT plasmids that either coexpressed EHBP1 RNAi (EHBP1 RNAi/GFP-EHBP1 and EHBP1 RNAi/GFP-EHBP1$^{399–722}$), contained a scrambled RNAi sequence (Scr. RNAi/GFP-EHBP1 and Scr. RNAi/GFP-EHBP1$^{399–722}$), and lacked any inserted RNAi sequence (-/GFP-EHBP1 and -/GFP-EHBP1$^{399–722}$), respectively. Quantitative data for GFP-EHBP1 (***A***) and GFP-EHBP1$^{399–722}$ (***B***) were normalized to anti-GAPDH signals (representing cell numbers) and depicted in relation to Scr. RNAi control data. $n = 3$ independent experiments each. Data, mean ± SEM in the form of bar plots and dot plots (red). For visual validation of EHBP1 knockdown in hippocampal neurons, see Figure 3*C*. ***C***, Representative MIPs of rat hippocampal neurons transfected with either (GFP-reported) Scr. RNAi or EHBP1 RNAi and Imaris reconstructions of neuronal morphology. Scale bars, 10 µm. ***D–H***, Quantitative determinations of specific defects in dendritic arborization caused by EHBP1 deficiency by addressing dendritic branching points (***D***), dendritic terminal points (***E***), and total dendritic tree length (***F***), as well as by conducting Sholl analyses (***G***) and dendritic branch depth analyes (***H***). Data, mean ± SEM. Scr. RNAi, $n = 40$; EHBP1 RNAi, $n = 40$ neurons from 4 independent coverslips and 2 independent neuronal preparations. Student's *t* test (***D–F***) and two-way ANOVA with Sidak posttest (***G***,***H***). *$p < 0.05$; **$p < 0.01$; ***$p < 0.001$; ****$p < 0.0001$ (exact *p* values are provided directly in the figure panels ***D–F***; note that *p* values <0.0001 are not reported by Prism 6 software).

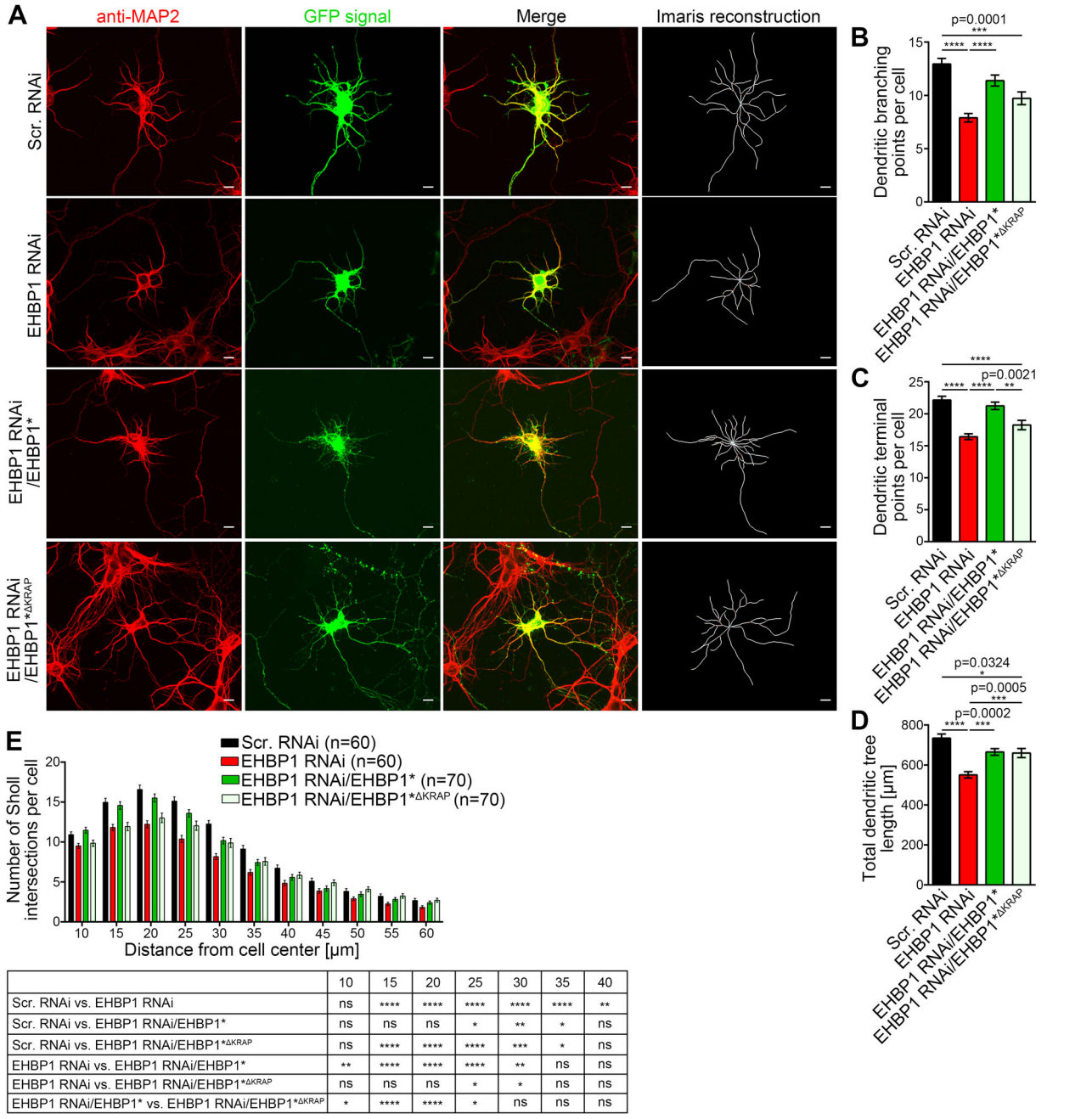


| | 10 | 15 | 20 | 25 | 30 | 35 | 40 |
|---|---|---|---|---|---|---|---|
| Scr. RNAi vs. EHBP1 RNAi | ns | **** | **** | **** | **** | **** | ** |
| Scr. RNAi vs. EHBP1 RNAi/EHBP1* | ns | ns | ns | * | ** | * | ns |
| Scr. RNAi vs. EHBP1 RNAi/EHBP1*$^{\Delta KRAP}$ | ns | **** | **** | **** | *** | * | ns |
| EHBP1 RNAi vs. EHBP1 RNAi/EHBP1* | ** | **** | **** | **** | ** | ns | ns |
| EHBP1 RNAi vs. EHBP1 RNAi/EHBP1*$^{\Delta KRAP}$ | ns | ns | ns | * | * | ns | ns |
| EHBP1 RNAi/EHBP1* vs. EHBP1 RNAi/EHBP1*$^{\Delta KRAP}$ | * | **** | **** | * | ns | ns | ns |

**Figure 7.** The EHBP1 loss-of-function phenotype in dendritic branching can be rescued by reexpression of EHBP1 but not of an EHBP1 mutant unable to associate with syndapin I. ***A***, Representative MIPs of primary rat hippocampal neurons transfected (at DIV4; fixed 40 h later) with Scr. RNAi coexpressing GFP, EHBP1 RNAi coexpressing GFP, EHBP1 RNAi coexpressing a silently mutated, EHBP1 RNAi-insensitive, GFP-tagged EHBP1 (EHBP1 RNAi/EHBP1*), and EHBP1 RNAi-coexpressing GFP-EHBP1*$^{\Delta KRAP}$ (EHBP1 RNAi/EHBP1*$^{\Delta KRAP}$), that is, a mutant lacking the identified syndapin I binding interface, respectively (for immunoblotting and integrity analyses of GFP-EHBP1$^{\Delta KRAP}$ versus wild-type GFP-EHBP1, see Fig. 3*K*). Shown are anti-MAP2 immunostainings, GFP signals, merged signals and 3D reconstructions of neuronal morphologies by Imaris. Scale bars, 10 µm. ***B–E***, Quantitative determinations of specific defects in dendritic arborization and putative rescue effects by addressing dendritic branching points (***B***), dendritic terminal points (***C***), and the summarized length of the dendritic arbor (***D***) and by Sholl analyses (***E***). Data are mean ± SEM. Scr. RNAi, $n = 60$; EHBP1 RNAi, $n = 60$; EHBP1 RNAi/EHBP1*, $n = 70$; EHBP1 RNAi/EHBP1*$^{\Delta KRAP}$, $n = 70$ neurons of 6–7 independent coverslips and 3 independent neuronal preparations. One-way ANOVA with Tukey's posttest (***B–D***) and two-way ANOVA with Sidak posttest (***E***). *$p < 0.05$; **$p < 0.01$; ***$p < 0.001$; ****$p < 0.0001$ (exact $p$ values are provided directly in the figure panels (except for Sholl analyses); note that $p$ values <0.0001 are not reported by Prism 6 software).

and the actin nucleator Cobl at dendritic branch sites supported this view (Fig. 11). Syndapin I interacts with the plasma membrane (Dharmalingam et al., 2009) and specifically prefers/induces membrane areas with curved topology, such as those found at nascent dendritic branch sites (Izadi et al., 2021). Furthermore, syndapin I does not provide a general association to actin filaments but specifically functionally and physically couples to actin filament formation by associations with the actin nucleator Cobl (Schwintzer et al., 2011) and its ancestor Cobl-like (Izadi et al., 2021) as well as with the neural Wiskott–Aldrich–Syndrome protein (N-WASP; Qualmann et al., 1999; Dharmalingam et al., 2009). Syndapin I could therefore perhaps integrate these effectors into EHBP1-mediated dendritic arborization.

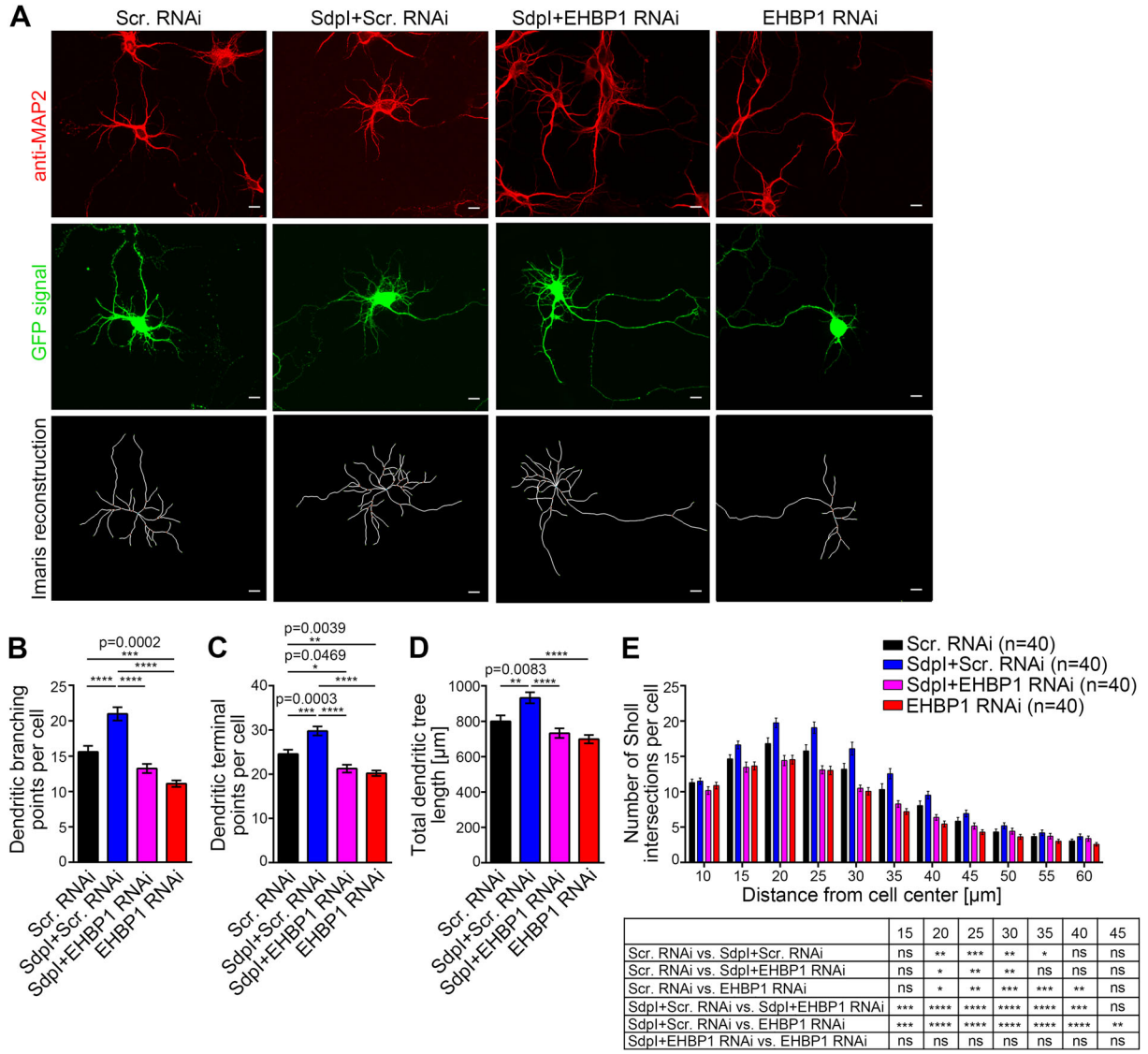


| | 15 | 20 | 25 | 30 | 35 | 40 | 45 |
|---|---|---|---|---|---|---|---|
| Scr. RNAi vs. SdpI+Scr. RNAi | ns | ** | *** | ** | * | ns | ns |
| Scr. RNAi vs. SdpI+EHBP1 RNAi | ns | * | ** | ** | ns | ns | ns |
| Scr. RNAi vs. EHBP1 RNAi | ns | * | ** | *** | *** | ** | ns |
| SdpI+Scr. RNAi vs. SdpI+EHBP1 RNAi | *** | **** | **** | **** | **** | *** | ns |
| SdpI+Scr. RNAi vs. EHBP1 RNAi | *** | **** | **** | **** | **** | **** | ** |
| SdpI+EHBP1 RNAi vs. EHBP1 RNAi | ns | ns | ns | ns | ns | ns | ns |

**Figure 8.** Syndapin I-mediated dendritic arbor formation requires EHBP1. ***A***, MIPs of primary rat hippocampal neurons that were transfected with (GFP-reported) RNAi plasmids and with Xpress-syndapin I-encoding plasmids as indicated and Imaris reconstructions of dendritic morphology. Scale bars, 10 µm. ***B–E***, Quantitative determinations of the key dendritic arborization parameters dendritic branching points (***B***), dendritic terminal points (***C***), and total dendritic length (***D***) as well as Sholl analyses (***E***) demonstrating that dendritic arborization promoted by syndapin I is dependent on EHBP1. Data, mean ± SEM. Scr. RNAi, $n = 40$; SdpI+Scr. RNAi, $n = 40$; SdpI+EHBP1 RNAi, $n = 40$; EHBP1 RNAi, $n = 40$ neurons from 4 independent coverslips and 2 independent neuronal preparations. One-way ANOVA with Tukey posttest (***B–D***) and two-way ANOVA with Sidak posttest for Sholl analysis (***E***). *$p < 0.05$; **$p < 0.01$; ***$p < 0.001$; ****$p < 0.0001$ (exact $p$ values are provided directly in the figure panels (except for Sholl analyses); note that $p$ values <0.0001 are not reported by Prism 6 software).

Yet, to our surprise, EHBP1 seemed to be able to promote some dendritic arborization even in an N-WASP-deficient background (GFP-EHBP1+N-WASP RNAi; Fig. 12*A–E*). None of the diminished dendritic parameters caused by N-WASP RNAi were observable in cells cotransfected with GFP-EHBP1. On the other hand, GFP-EHBP1+N-WASP RNAi neurons also did not display the elevated dendritic arborization determined for EHBP1 gain-of-function (GFP-EHBP1+Scr. RNAi). Instead, the determined dendritic parameters of GFP-EHBP1+N-WASP RNAi neurons seem to represent additive combinations of the promoting effects of EHBP1 and inhibitory effects of N-WASP deficiency (Fig. 12*A–E*).

Such quantitative data neither formally dismiss an involvement of N-WASP in EHBP1-mediated dendritic branching nor provide any formal proof for the critical role of N-WASP. They most likely represent a scenario in which N-WASP functions in EHBP1-mediated dendritic arborization are secured by partial redundancy with another effector and/or EHBP1 and N-WASP mostly work in parallel rather than in one molecular process.

In addition to N-WASP and the Arp2/3 complex, syndapin I can also functionally couple to the actin nucleator Cobl (Ahuja et al., 2007; Schwintzer et al., 2011). We therefore next addressed the putative role of Cobl in EHBP1-mediated dendritic arborization (Fig. 12*A,F–I*). Stunningly, in contrast to N-WASP RNAi, Cobl RNAi completely suppressed EHBP1-mediated dendritogenesis. Quantitative analyses revealed that dendritic branch point numbers, terminal point numbers, and the total dendritic tree length of EHBP1 and Cobl RNAi-expressing neurons were showing a highly statistically significant decrease not only when compared to GFP-EHBP1+Scr. RNAi (all three parameters $p < 0.0001$; ****) but, in contrast to the results of the study of the N-WASP involvement, also when compared to control (GFP+Scr. RNAi; Fig. 12*F–I*).

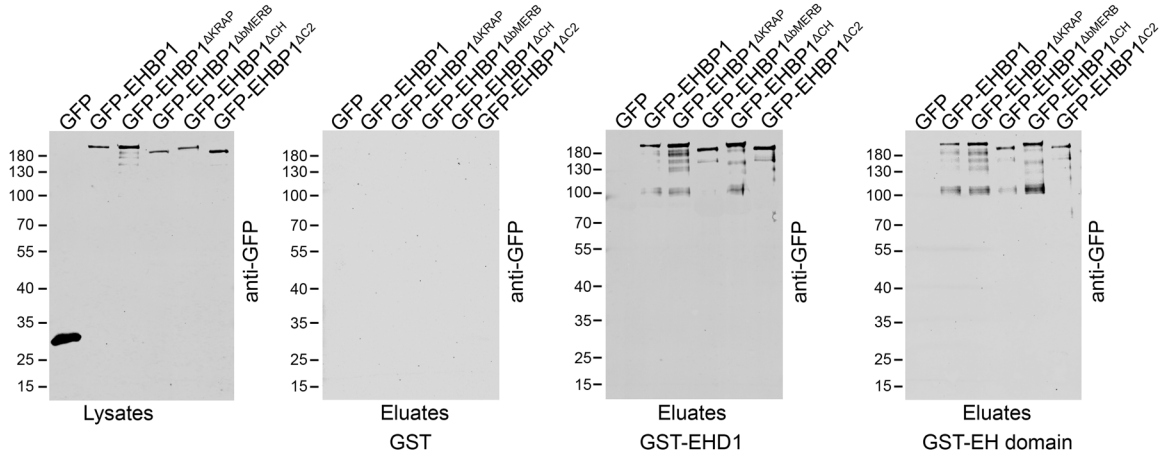


**Figure 9.** Also EHBP1 mutants lacking the C2 domain, the CH domain, and the bMERB domain, respectively, readily associate with the established EHBP1 interaction partner EHD1. Immunoblotting analyses of coprecipitation experiments with GFP, GFP-EHBP1, and GFP-EHBP1 deletion mutants lacking the specified domains and motifs and with immobilized, recombinant GST, GST-EHD1, and GST-EH domain of EHD1 showing the integrity and the ability of GFP-EHBP1 mutants lacking the C2 domain, the CH domain, and the bMERB domain, respectively, to readily associate with EHD1 and its EH domain, respectively (see eluates).

Importantly, the dendritic parameters of EHBP1 and Cobl RNAi-coexpressing neurons hereby were so low that they were indistinguishable from those determined for Cobl RNAi, that is, the promotion of dendritic arborization by EHBP1 was completely suppressed when Cobl was lacking (Fig. 12*F–H*). This complete suppression of EHBP1-mediated dendritic branching was observed throughout the entire dendritic arbor of the developing neurons (Fig. 12*I*) and demonstrated a strict requirement of the actin nucleator Cobl for EHBP1-mediated dendritic arborization.

### Syndapin I can interconnect EHBP1 with Cobl

The complete suppression of EHBP1 functions in dendritic arborization by knockdown of the actin nucleator Cobl suggested a direct involvement of Cobl in the dendritic functions of EHBP1. Since, via its C-terminal SH3 domain, syndapin I only can either bind EHBP1 (Figs. 1, 2) or associate with the actin nucleator Cobl (Schwintzer et al., 2011), but using its N-terminal F-BAR domain syndapin I can self-associate (Kessels and Qualmann, 2006), we hypothesized that syndapin I could bring about the critical involvement of Cobl in EHBP1-mediated dendritic arborization by formation of ternary protein complexes composed of EHBP1, syndapin I, and Cobl. Indeed, both syndapin I and GFP-Cobl were coprecipitated with GST-EHBP1$^{267–394}$, and this EHBP1/Cobl association did not occur when syndapin I was absent (Fig. 12*J*).

The indirect association of Cobl to EHBP1 was specific, as it did not occur when merely GFP was offered (Fig. 12*J*). It also did not occur in control experiments using merely GST (Fig. 12*K*).

Surprisingly, no syndapin I-mediated complex formation of EHBP1 with GFP-N-WASP$^{265–501}$—an N-WASP deletion mutant that includes a readily accessible proline-rich domain of N-WASP, which has been demonstrated to associate with syndapin I (Kessels and Qualmann, 2002)—was detected (Fig. 12*J*).

In contrast, Cobl-like, which cooperates with Cobl in a syndapin I-dependent manner (Izadi et al., 2021), also was specifically detectable in ternary complexes with EHBP1 and syndapin I and thereby resembled Cobl (Fig. 12*J,K*). The detected interactions of EHBP1 with Cobl and Cobl-like, respectively, required the presence of syndapin I (Fig. 12*J,K*). Syndapin I thus interconnects EHBP1 with factors leading to local F-actin formation.

## Discussion

The data presented here revealed a function of EHBP1 in the development of proper neuronal cell shape. In line with this function, EHBP1 transiently occurs at dendritic branch induction sites and accumulates at such sites prior to dendritic branch induction. Despite the strong enrichment of EHBP1 in the vertebrate brain, surprisingly little had previously been reported about functional roles and interactions of EHBP1 in neurons. Our molecular studies as well as our gain-of-function and loss-of-function studies furthermore show that EHBP1's role in dendritic arborization involves an association with syndapin I, as identified by a genome-wide in silico screening approach, and coordination with actin cytoskeletal functions, as uncovered by biochemical and functional studies.

Surprisingly, the identified EHBP1 functions in neuronal morphology development did not require the bMERB domain, which had been shown to mediate interactions with several Rab GTPases (Shi et al., 2010; Rai et al., 2016, 2020), as demonstrated by our loss-of-function and rescue experiments. Strikingly, while all the other EHBP1 mutants examined failed to rescue the EHBP1 deficiency phenotypes in dendritic arbor development, solely GFP-EHBP1$^{\Delta bMERB}$ was able to rescue the EHBP1 loss-of-function phenotypes quantitatively. A close functional relationship and importance of EHBP1 complexes with Rab proteins were reported to regulate vesicular trafficking, endosomal tubulation, lipophagy, Notch signaling, and developmental and behavioral phenotypes (Shi et al., 2010; Giagtzoglou et al., 2012, 2013; Li et al., 2016; Wang et al., 2016; Nakamura et al., 2020; Farmer et al., 2021). Furthermore, several Rab GTPases including the identified EHBP1-binding partners Rab5 (Satoh et al., 2008; Mori et al., 2013), Rab8 (Huber et al., 1995), Rab10 (Taylor et al., 2015; Zou et al., 2015), and Rab11 (Lazo et al., 2013; Siri et al., 2020) were described to play some role in dendritic outgrowth and arborization (Shikanai et al., 2018). In neuronal cells of *C. elegans*, EHBP1 was reported to function with Rab10 during trafficking of the glutamate receptor GLR-1 from endosomal compartments to synaptic membranes since *ehbp1-1* mutant animals phenocopied *rab-10* mutants (Shi et al., 2010). EHBP1 also regulated the subcellular localization of Rab10 (Shi et al., 2010). Defects in synapse formation, however, were not detected (Shi et al., 2010). It is important to note,

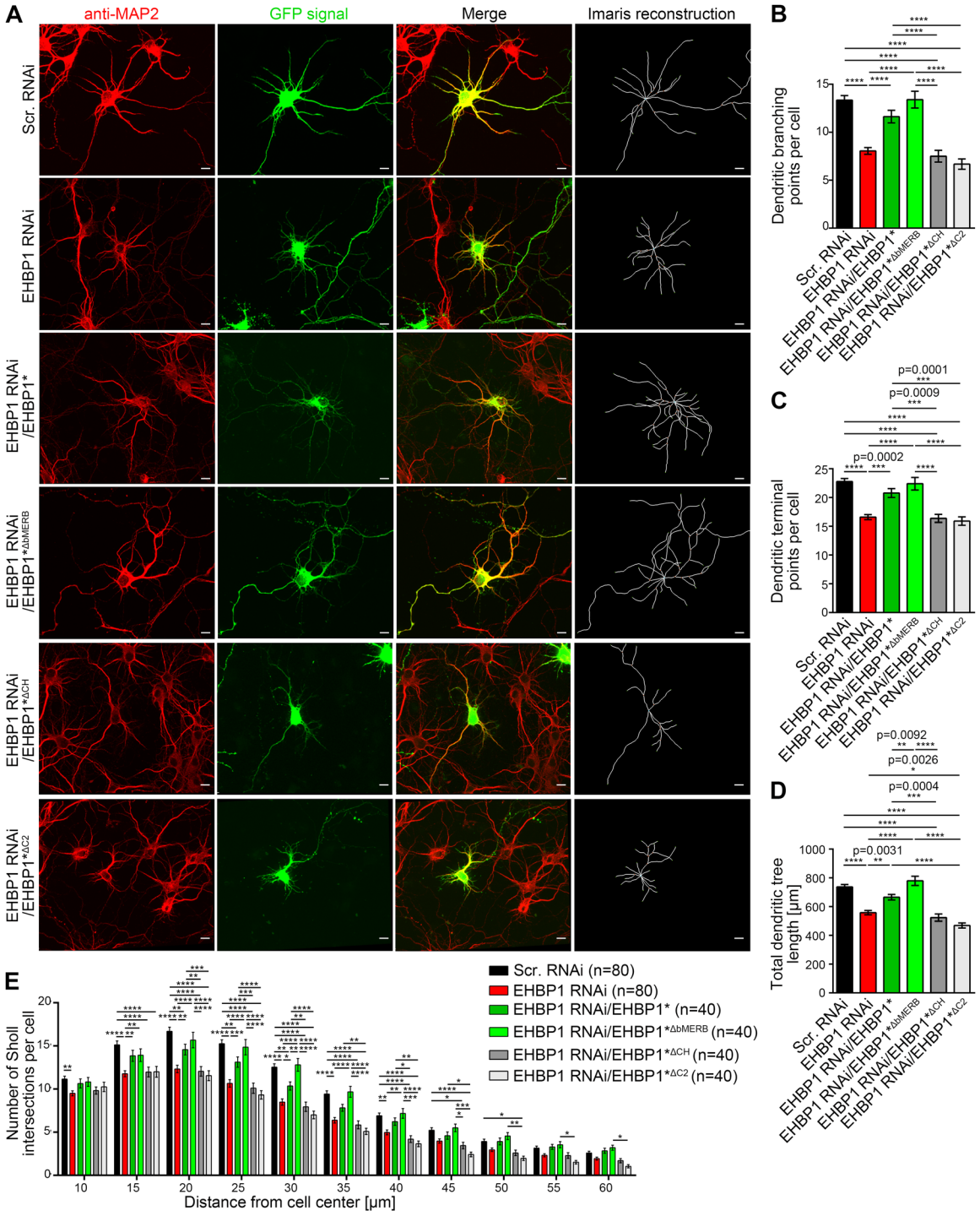


**Figure 10.** EHBP1 functions in neuronal arborization also critically involve the C2 and CH domains of EHBP1 but not the C-terminal bMERB domain. ***A***, Representative MIPs of DIV6 primary rat hippocampal neurons transfected at DIV4 with Scr. RNAi, EHBP1 RNAi, EHBP1 RNAi/EHBP1*, and EHBP1 RNAi plasmids, which do not coexpress wild-type GFP-EHBP1* but mutants lacking the bMERB domain (EHBP1 RNAi/EHBP1*$^{\Delta bMERB}$), the CH domain (EHBP1 RNAi/EHBP1*$^{\Delta CH}$), and the C2 domain (EHBP1 RNAi/EHBP1*$^{\Delta C2}$), respectively. Besides the immunofluorescence images of anti-MAP2 signals, the GFP signals and the merged images, also 3D reconstructions of neuronal morphologies by Imaris are shown. Scale bars, 10 µm. ***B–E***, Quantitative determinations of dendritic parameters in the rescue attempts of EHBP1 loss-of-function with a variety of EHBP1 mutants. Note that reexpression of EHBP1*$^{\Delta CH}$ and EHBP1*$^{\Delta C2}$ failed to rescue the EHBP1 loss-of-function phenotypes, whereas EHBP1* and EHBP1*$^{\Delta bMERB}$ fully rescued the dendritic parameters affected by EHBP1 RNAi. Data are mean ± SEM. Scr. RNAi, $n = 80$; EHBP1 RNAi, $n = 80$; EHBP1 RNAi/EHBP1*, $n = 40$; EHBP1 RNAi/EHBP1*$^{\Delta bMERB}$, $n = 40$; EHBP1 RNAi/EHBP1*$^{\Delta CH}$, $n = 40$; and EHBP1 RNAi/EHBP1*$^{\Delta C2}$, $n = 40$ transfected neurons from 4–8 independent coverslips and 2–4 independent neuronal preparations. One-way ANOVA with Tukey's posttest (***B–D***) and two-way ANOVA with Sidak posttest (***E***), respectively. *$p < 0.05$; **$p < 0.01$; ***$p < 0.001$; ****$p < 0.0001$. Except for Sholl analyses, the exact $p$ values are provided directly in the figure panels; note that $p$ values <0.0001 are not reported by Prism 6 software.

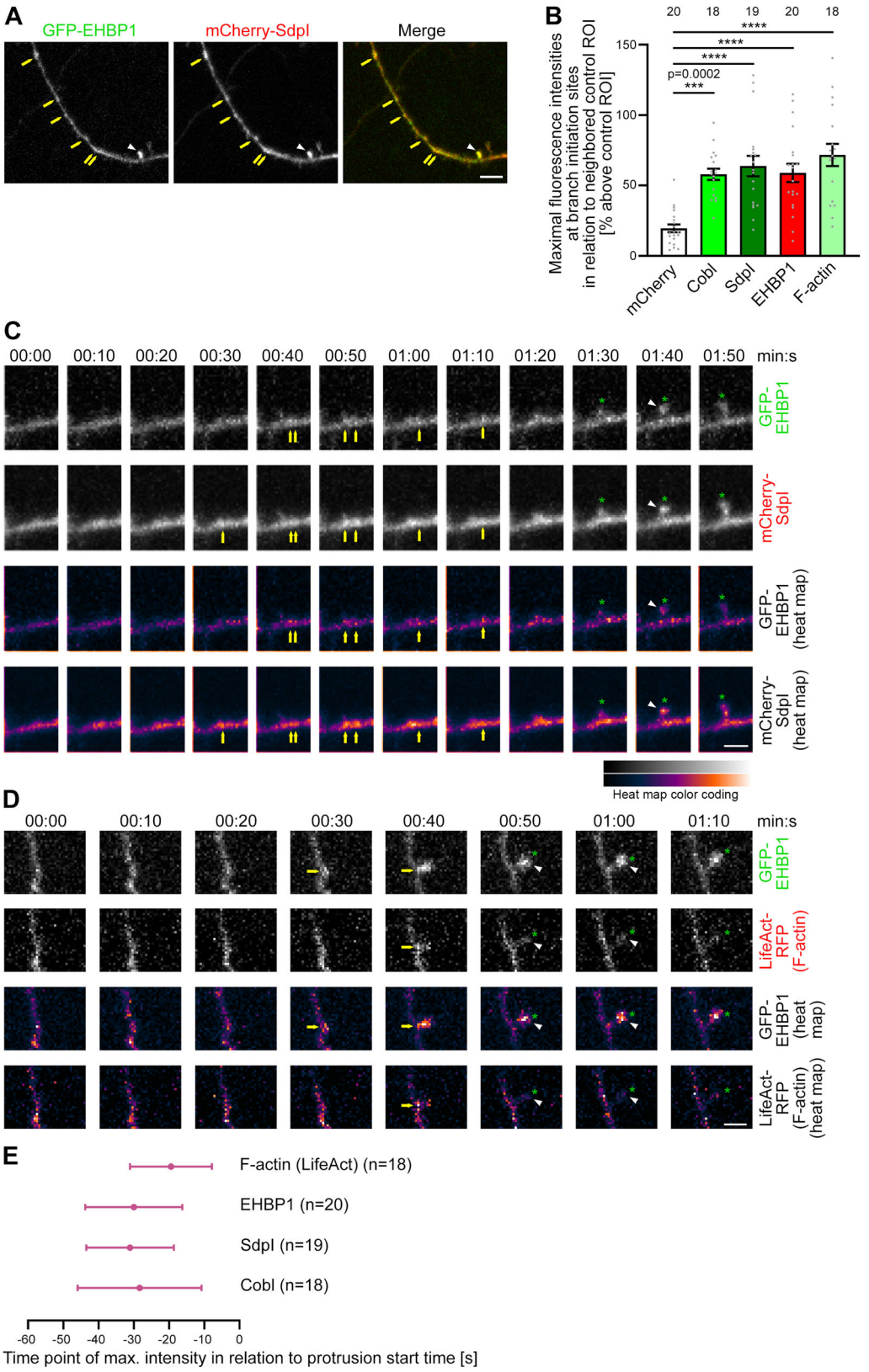


**Figure 11.** Continued.

however, that in *C. elegans*, EHBP1 lacks many features that EHBP1 seems to have acquired later in evolution. Compared to mammalian EHBP1, it lacks the C-terminal CaaX box, which represents a target for farnesylation (Rai et al., 2020) for meditating membrane anchoring. *C. elegans* EHBP1 notably also lacks NPF motifs responsible for binding to EHD proteins—its name-giving interaction identified in mammals (Guilherme et al., 2004a). Consistently, *C. elegans* EHBP1 did not interact with RME-1, the *C. elegans* ortholog (Shi et al., 2010).

Importantly, our studies uncovered a thus far unrecognized binding motif in EHBP1 that is important for proper EHBP1 function in mammalian neurons—the KRAP motif revealed by our in silico interaction screen using a syndapin I SH3 domain binding consensus deduced from the syndapin binding sites of Cobl and Cobl-like (Schwintzer et al., 2011; Izadi et al., 2021). The KRAP motif of EHBP1 additionally shares similarities with other defined syndapin I binding sites, such as those in dynamin I (Anggono and Robinson, 2007), ProSAP1/Shank2 (Schneider et al., 2014), and the glycine receptor beta subunit (del Pino et al., 2014; Tröger et al., 2022) further supporting the validity of the in silico interaction screening approach.

Strikingly, we discovered this thus far unrecognized binding motif only in EHBP1 proteins of chordates, but not in EHBP1 proteins of insects (such as *Drosophila melanogaster* or *Apis mellifera*) or of worms (e.g., *C. elegans*). The evolutionary acquisition of an additional amino acid motif in EHBP1 proteins obviously allowed for the expansion and/or specification of EHBP1 protein functions by complex formation with syndapins. Coimmunoprecipitations of endogenous EHBP1 with syndapin I from rat brain lysates and recruitment of endogenous EHBP1 to syndapin I-enriched sites in primary hippocampal neurons clearly demonstrate that EHBP1/syndapin I complexes are indeed formed in the brain and intact neuronal cells.

Syndapins are F-BAR superfamily proteins. Their membrane curvature-generating properties shape distinct membrane areas into specific topologies. Additionally, syndapins recruit and activate cytoskeletal effectors providing forces for further membrane deformation and structural confinements (Dharmalingam et al., 2009; Schwintzer et al., 2011; Schneider et al., 2014; Izadi et al., 2021).

The close functional cooperation of EHBP1 and syndapin I during the dendritogenesis of developing neurons is supported by several lines of evidence. First, EHBP1 and syndapin I show remarkably similar and precise spatiotemporal colocalizations at nascent dendritic branch sites, at which both proteins accumulated prior to dendritic branch formation. Second, EHBP1-mediated dendritic arborization was critically dependent on the identified syndapin I binding interface, as EHBP1$^{\Delta KRAP}$ failed to elicit any surplus of dendritic arborization. Third, explicitly addressing a requirement of syndapin I for EHBP1-mediated dendritic arborization, EHBP1 gain-of-function phenotypes were strictly dependent on the presence of syndapin I. Fourth, while the EHBP1 loss-of-function phenotype in dendritic branching was rescued by reexpression of EHBP1, reexpression of an EHBP1 mutant unable to directly associate with syndapin I was not capable of rescuing the EHBP1 loss-of-function phenotypes in dendritic arbor formation. Furthermore, fifth, our analyses show that *vice versa* syndapin I-mediated dendritic arbor formation requires EHBP1.

EHBP1 contains a central CH domain that associates with actin filaments (Shi et al., 2010), an interaction promoted by the binding of Rab GTPases, which are thought to relieve an intramolecular autoinhibitory interaction of the bMERB domain to the CH domain (Wang et al., 2016; Rai et al., 2020). Our functional studies clearly show the importance of EHBP1's CH domain, since EHBP1$^{\Delta CH}$ was unable to rescue defects in dendritic arbor development caused by EHBP1 deficiency. However, CH domain-mediated, static associations with filamentous actin appear insufficient to explain the role of EHBP1 in dendritic branching and outgrowth, as this would rather require some linkage to local F-actin formation. Our analyses provide a molecular mechanistic explanation of how this can be brought about. By the identified EHBP1 interaction with syndapin I, such a functional linkage to F-actin formation can be provided. Syndapin I binds and regulates several factors important for the de novo formation of actin filaments, the Arp2/3 complex activator N-WASP (Qualmann et al., 1999), the actin nucleator Cobl (Ahuja et al., 2007; Schwintzer et al., 2011), and Cobl-like (Izadi et al., 2018, 2021). Importantly, syndapin I has hereby been shown to functionally cooperate with N-WASP (Dharmalingam et al., 2009), Cobl (Schwintzer et al., 2011; Hou et al., 2015), and Cobl-like (Izadi et al., 2021) in dendritic arborization. Interestingly, functional experiments in neurons demonstrated that EHBP1 functions in dendritic arborization specifically rely on the syndapin I binding partner Cobl, but not on N-WASP. In line, our biochemical experimentation clearly showed that syndapin I readily interconnects EHBP1 with Cobl and Cobl-like but integration of N-WASP into EHBP1-containing ternary complexes was not

←

**Figure 11.** 3D time-lapse analyses show a spatiotemporal overlap of EHBP1 with its binding partner syndapin I, with the actin nucleator Cobl, and with F-actin during dendritic branch formation processes in developing primary rat hippocampal neurons. ***A***, Colocalization of GFP-EHBP1 and mCherry-syndapin I in a dendrite of a developing hippocampal neuron (transfection DIV6 and imaged 22 h thereafter). Arrows, accumulations of EHBP1 and syndapin I at sites along the dendrite. White arrowhead, EHBP1 and syndapin I accumulation inside of a short dendritic branch. Bar, 5 µm. ***B***, Quantitative determinations of maximal fluorescence intensities of GFP-EHBP1, mCherry-syndapin I, mCherry-Cobl, and LifeAct-RFP at nascent dendritic branch sites in relation to signals inside of control ROIs at non-branching dendritic sites (mCherry and GFP-EHBP1 data as in Fig. 5). Data, mean ± SEM and individual data points. mCherry and GFP-EHBP1 (EHBP1), $n = 20$ determinations in 10 and 5 transfected neurons, respectively; mCherry-Cobl (Cobl), $n = 18$ determinations in 11 transfected neurons; mCherry-syndapin I (SdpI), $n = 19$ determinations in 8 transfected neurons and LifeAct-RFP (F-actin) and 18 determinations in 5 transfected neurons (from at least 2 independent neuronal preparations each). ***C***, Image gallery (MIPs) of 12 individual frames of a 3D time-lapse analysis of GFP-EHBP1 and mCherry-syndapin I at nascent dendritic branch sites of developing hippocampal neurons transfected at DIV6 and imaged 22 h thereafter using a spinning disc microscope with a frame rate of 10 s per image stack. Shown are black and white representations of fluorescence (upper two panels) and false-color (*gem;* for heat map color coding, see legend) heat map representations (lower panels) of both proteins at nascent dendritic branch sites. Green asterisks track the tip position of the growing protrusion. Arrows mark protein accumulations at the nascent dendritic branch site and white arrowheads mark the accumulation of both EHBP1 and syndapin I inside of a newly formed dendritic branch during the first seconds of its outgrowth (see the 01:40 min:s frame). Bar, 2 µm. ***D***, Similar image gallery of eight individual frames of a 3D time-lapse analysis of a developing hippocampal neuron transfected at DIV6 with GFP-EHBP1 and LifeAct-RFP to highlight F-actin and imaged 17 h later. Markings as in ***C***. Bar, 2 µm. ***E***, Quantitative determinations of time points of maximal fluorescence intensities of GFP-EHBP1 (EHBP1), mCherry-syndapin I (SdpI), mCherry-Cobl (Cobl), and LifeAct (F-actin) at nascent dendritic branch sites in temporal relation to protrusion start (normalized to signals inside of control ROIs at neighboring, non-branching dendritic sites). Data, mean ± SEM. LifeAct, $n = 18$; EHBP1, $n = 20$; SdpI, $n = 19$; Cobl, $n = 18$ relative fluorescence profiles at dendritic branch sites from 5–11 transfected neurons from 2–5 independent preparations of primary neuronal cultures. One-way ANOVA with Tukey's posttest (***B***). ***$p < 0.001$; ****$p < 0.0001$ ($p$ values are shown in the figure; note that $p$ values <0.0001 are not reported by Prism 6 software).

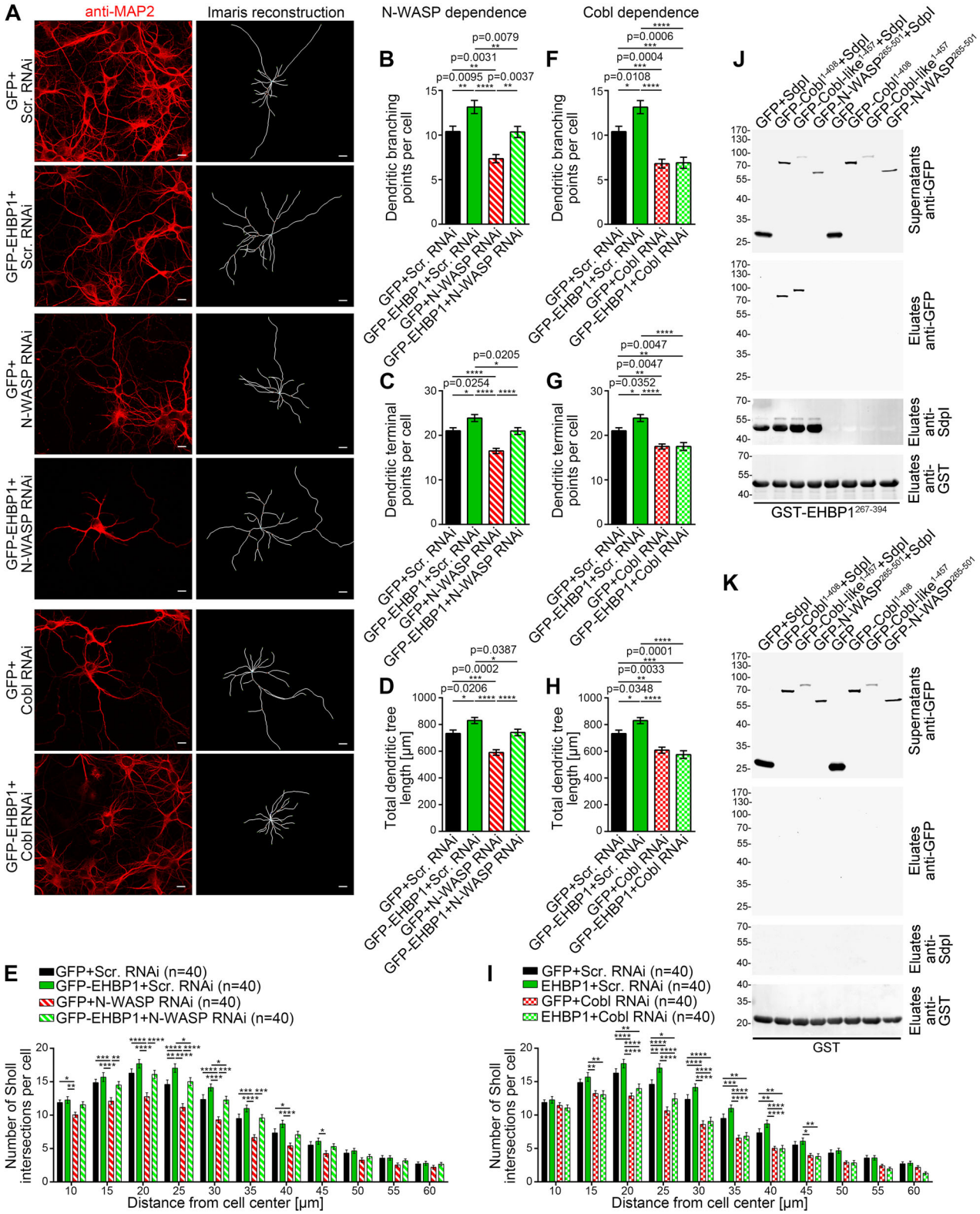


**Figure 12.** EHBP1 functions in dendritic arbor formation rely on the syndapin I binding partner Cobl. ***A***, MIPs of neurons that were cotransfected with the following combinations of plasmids, GFP+Scr. RNAi, GFP-EHBP1+Scr. RNAi, GFP+N-WASP RNAi, GFP-EHBP1+N-WASP RNAi, GFP+Cobl RNAi, and GFP-EHBP1+Cobl RNAi, respectively, at DIV4 and fixed 40 h thereafter (RNAi plasmids are CherryF-reported). Scale bars, 10 µm. ***B–I***, Quantitative determinations of dendritic branching points (***B***,***F***), dendritic terminal points (***C***,***G***), and total dendritic length (***D***,***H***) promoted by EHBP1 for their dependence on the syndapin I-binding Arp2/3 complex activator N-WASP (***B–E***) and on the syndapin I-binding actin nucleator Cobl (***F–I***), respectively. ***E***,***I***, Corresponding Sholl analyses. GFP+Scr. RNAi and GFP-EHBP1+Scr. RNAi data are repeated for each of the two quantitative analyses of dependence. Data, mean ± SEM. GFP+Scr. RNAi, $n = 40$; GFP-EHBP1+Scr. RNAi, $n = 40$; GFP+N-WASP RNAi, $n = 40$; GFP-EHBP1+N-WASP RNAi, $n = 40$; GFP+Cobl RNAi, $n = 40$; GFP-EHBP1+Cobl RNAi, $n = 40$ neurons from 4 independent coverslips and 2 independent neuronal preparations. One-way ANOVA with Tukey's posttest (***B–D***, ***F–H***) and two-way ANOVA with Sidak posttest (***E***,***I***), respectively. *$p < 0.05$; **$p < 0.01$; ***$p < 0.001$; ****$p < 0.0001$ (except for Sholl analyses, the exact $p$ values are provided directly in the figure panels; note that $p$ values <0.0001 are not reported by Prism 6 software). ***J***,***K***, Immunoblotting analyses of the supernatants (upper panels) and eluates (lower three panels) of coprecipitation experiments uncovering specific and syndapin I-dependent formation of complexes composed of immobilized GST-EHBP1$^{267–394}$, syndapin I, and GFP-Cobl and GFP-Cobl-like, respectively (***J***), and corresponding control experiments with immobilized GST (***K***). Note that EHBP1/syndapin I complexes additionally containing GFP-N-WASP were not detected by anti-GFP immunoblotting but GFP-N-WASP$^{265–501}$ completely remained in the supernatant.

detected. Consistently, Cobl and Cobl-like closely cooperate in dendritogenesis (Izadi et al., 2021). The here identified ability of syndapin I to physically bridge EHBP1 with Cobl and Cobl-like, respectively, is plausible considering syndapin I's F-BAR domain-mediated self-association ability (Kessels and Qualmann, 2006; Shimada et al., 2007; Wang et al., 2009). This mechanism leaves the SH3 domain of each syndapin I free for recruiting and coordinating (different) effector proteins. In line, our time-lapse analyses of dendritic arbor formation showed both a Cobl and an F-actin accumulation at branch induction sites and Cobl exhibited the same temporal profile as EHBP1 and syndapin I.

In order to support the initiation and outgrowth of new protrusive structures for dendritic arborization, actin filament formation factors have to be specifically targeted not only to the plasma membrane in general but particularly to branch initiation sites. In general, membrane association of EHBP1 can be mediated by a C-terminal CaaX box being a target for farnesylation in higher eukaryotes (Rai et al., 2020) and by an N-terminal C2 domain, which binds to different negatively charged phospholipids, as reported for human and worm EHBP1 (Wang et al., 2016; Rai et al., 2020). However, neither of these molecular properties can explain the observed specific targeting of EHBP1 proteins to branch induction sites. The membrane-shaping protein syndapin I specifically occurred at the base of nascent membrane protrusions of developing neurons (this study; Hou et al., 2015; Izadi et al., 2021). Such a specific localization to the curved membrane areas at dendritic branch induction sites allows for coordinating effector functions in dendritic branch induction in a spatially defined manner. Indeed, electron microscopic analyses at freeze-fractured plasma membranes demonstrated that syndapin I enriching at such curved membrane surfaces occurred in the form of nanoclusters (Izadi et al., 2021). Syndapin I thus seems to play a dual role in EHBP1-mediated dendritic arborization and provides distinct, specific membrane as well as actin cytoskeletal interactions. Our study demonstrates that this identified molecular and functional interaction between EHBP1 and syndapin I evolutionally arose with the occurrence of KRAP motifs in EHBP1 proteins in chordates and is indispensable for obtaining proper cell shape during the neuronal development of these higher animals.

## References


Ahuja R, Pinyol R, Reichenbach N, Custer L, Klingensmith J, Kessels MM, Qualmann B (2007) Cordon-bleu is an actin nucleation factor and controls neuronal morphology. Cell 131:337–350.

Anggono V, Robinson PJ (2007) Syndapin I and endophilin I bind overlapping proline-rich regions of dynamin I: role in synaptic vesicle endocytosis. J Neurochem 102:931–943.

Braun A, Pinyol R, Dahlhaus R, Koch D, Fonarev P, Grant BD, Kessels MM, Qualmann B (2005) EHD proteins associate with syndapin I and II and such interactions play a crucial role in endosomal recycling. Mol Biol Cell 16:3642–3658.

Carlin RK, Grab DJ, Cohen RS, Siekevitz P (1980) Isolation and characterization of postsynaptic densities from various brain regions: enrichment of different types of postsynaptic densities. J Cell Biol 86:831–845.

del Pino I, Koch D, Schemm R, Qualmann B, Betz H, Paarmann I (2014) Proteomic analysis of glycine receptor β subunit (GlyRbeta)-interacting proteins: evidence for syndapin I regulating synaptic glycine receptors. J Biol Chem 289:11396–11409.

Dharmalingam E, Haeckel A, Pinyol R, Schwintzer L, Koch D, Kessels MM, Qualmann B (2009) F-BAR proteins of the syndapin family shape the plasma membrane and are crucial for neuromorphogenesis. J Neurosci 29:13315–13327.

Farmer T, Xie S, Naslavsky N, Stöckli J, James DE, Caplan S (2021) Defining the protein and lipid constituents of tubular recycling endosomes. J Biol Chem 296:100190.

Giagtzoglou N, Li T, Yamamoto S, Bellen HJ (2013) Drosophila EHBP1 regulates Scabrous secretion during Notch-mediated lateral inhibition. J Cell Sci 126:3686–3696.

Giagtzoglou N, Yamamoto S, Zitserman D, Graves HK, Schulze KL, Wang H, Klein H, Roegiers F, Bellen HJ (2012) dEHBP1 controls exocytosis and recycling of Delta during asymmetric divisions. J Cell Biol 196:65–83.

Gudmundsson J, et al. (2008) Common sequence variants on 2p15 and Xp11.22 confer susceptibility to prostate cancer. Nat Genet 40:281–283.

Guilherme A, Soriano NA, Bose S, Holik J, Bose A, Pomerleau DP, Furcinitti P, Leszyk J, Corvera S, Czech MP (2004a) EHD2 and the novel EH domain binding protein EHBP1 couple endocytosis to the actin cytoskeleton. J Biol Chem 279:10593–10605.

Guilherme A, Soriano NA, Furcinitti PS, Czech MP (2004b) Role of EHD1 and EHBP1 in perinuclear sorting and insulin-regulated GLUT4 recycling in 3T3-L1 adipocytes. J Biol Chem 279:40062–40075.

Haag N, Schwintzer L, Ahuja R, Koch N, Grimm J, Heuer H, Qualmann B, Kessels MM (2012) The actin nucleator Cobl is crucial for Purkinje cell development and works in close conjunction with the F-actin binding protein Abp1. J Neurosci 32:17842–17856.

Homann J, et al. (2022) Genome-wide association study of Alzheimer's disease brain imaging biomarkers and neuropsychological phenotypes in the European medical information framework for Alzheimer's disease multimodal biomarker discovery dataset. Front Aging Neurosci 14:840651.

Hou W, Izadi M, Nemitz S, Haag N, Kessels MM, Qualmann B (2015) The actin nucleator Cobl is controlled by calcium and calmodulin. PLoS Biol 13:e1002233.

Hou W, Nemitz S, Schopper S, Nielsen ML, Kessels MM, Qualmann B (2018) Arginine methylation by PRMT2 controls the functions of the actin nucleator Cobl. Dev Cell 45:262–275.

Huber LA, Dupree P, Dotti CG (1995) A deficiency of the small GTPase rab8 inhibits membrane traffic in developing neurons. Mol Cell Biol 15:918–924.

Itoh T, Erdmann KS, Roux A, Habermann B, Werner H, De Camilli P (2005) Dynamin and the actin cytoskeleton cooperatively regulate plasma membrane invagination by BAR and F-BAR proteins. Dev Cell 9:791–804.

Izadi M, Schlobinski D, Lahr M, Schwintzer L, Qualmann B, Kessels MM (2018) Cobl-like promotes actin filament formation and dendritic branching using only a single WH2 domain. J Cell Biol 217:211–230.

Izadi M, Seemann E, Schlobinski D, Schwintzer L, Qualmann B, Kessels MM (2021) Functional interdependence of the actin nucleator Cobl and Cobl-like in dendritic arbor development. Elife 10:e67718.

Izadi M, Wolf D, Seemann E, Ori A, Schwintzer L, Steiniger F, Kessels MM, Qualmann B (2023) Membrane shapers from two distinct superfamilies cooperate in the development of neuronal morphology. J Cell Biol 222:e202211032.

Ji Y, Koch D, González Delgado J, Günther M, Witte OW, Kessels MM, Frahm C, Qualmann B (2021) Poststroke dendritic arbor regrowth requires the actin nucleator Cobl. PLoS Biol 19:e3001399.

Kessels MM, Qualmann B (2002) Syndapins integrate N-WASP in receptor-mediated endocytosis. EMBO J 21:6083–6094.

Kessels MM, Qualmann B (2006) Syndapin oligomers interconnect the machineries for endocytic vesicle formation and actin polymerization. J Biol Chem 281:13285–13299.

Koch D, et al. (2011) Proper synaptic vesicle formation and neuronal network activity critically rely on syndapin I. EMBO J 30:4955–4969.

Koch N, et al. (2020) Syndapin I loss-of-function in mice leads to schizophrenia-like symptoms. Cereb Cortex 30:4306–4324.

Lazo OM, Gonzalez A, Ascaño M, Kuruvilla R, Couve A, Bronfman FC (2013) BDNF regulates Rab11-mediated recycling endosome dynamics to induce dendritic branching. J Neurosci 33:6112–6122.

Li Z, et al. (2016) A novel Rab10-EHBP1-EHD2 complex essential for the autophagic engulfment of lipid droplets. Sci Adv 2:e1601470.

Matsumoto Y, et al. (2021) Detection of novel and recurrent conjoined genes in non-Hodgkin B-cell lymphoma. J Clin Exp Hematop 61:71–77.

Matthaeus C, Sochacki KA, Dickey AM, Puchow D, Haucke V, Lehmann M, Taraska JW (2022) The molecular organization of differentially curved caveolae indicates bendable structural units at the plasma membrane. Nat Commun 13:7234.

Mori Y, Matsui T, Fukuda M (2013) Rabex-5 protein regulates dendritic localization of small GTPase Rab17 and neurite morphogenesis in hippocampal neurons. J Biol Chem 288:9835–9847.

Nakamura Y, Ochi Y, Satoh T, Satoh AK (2020) Rab10, Crag and Ehbp1 regulate the basolateral transport of $Na^+K^+$ATPase in *Drosophila* photoreceptors. J Cell Sci 33:jcs238790.

Pinyol R, Haeckel A, Ritter A, Qualmann B, Kessels MM (2007) Regulation of N-WASP and the Arp2/3 complex by Abp1 controls neuronal morphology. PLoS One 2:e400.

Qualmann B, Boeckers TM, Jeromin M, Gundelfinger ED, Kessels MM (2004) Linkage of the actin cytoskeleton to the postsynaptic density via direct interactions of Abp1 with the ProSAP/Shank family. J Neurosci 24: 2481–2495.

Qualmann B, Kelly RB (2000) Syndapin isoforms participate in receptor-mediated endocytosis and actin organization. J Cell Biol 148:1047–1062.

Qualmann B, Roos J, DiGregorio PJ, Kelly RB (1999) Syndapin I, a synaptic dynamin-binding protein that associates with the neural Wiskott–Aldrich syndrome protein. Mol Biol Cell 10:501–513.

Rai A, Bleimling N, Vetter IR, Goody RS (2020) The mechanism of activation of the actin binding protein EHBP1 by Rab8 family members. Nat Commun 11:4187.

Rai A, Oprisko A, Campos J, Fu Y, Friese T, Itzen A, Goody RS, Gazdag EM, Müller MP (2016) bMERB domains are bivalent Rab8 family effectors evolved by gene duplication. Elife 5:e18675.

Satoh D, Sato D, Tsuyama T, Saito M, Ohkura H, Rolls MM, Ishikawa F, Uemura T (2008) Spatial control of branching within dendritic arbors by dynein-dependent transport of Rab5-endosomes. Nat Cell Biol 10: 1164–1171.

Schneider K, Seemann E, Liebmann L, Ahuja R, Koch D, Westermann M, Hubner CA, Kessels MM, Qualmann B (2014) ProSAP1 and membrane nanodomain-associated syndapin I promote postsynapse formation and function. J Cell Biol 205:197–215.

Schwintzer L, Koch N, Ahuja R, Grimm J, Kessels MM, Qualmann B (2011) The functions of the actin nucleator Cobl in cellular morphogenesis critically depend on syndapin I. EMBO J 30:3147–3159.

Shi A, Chen CC, Banerjee R, Glodowski D, Audhya A, Rongo C, Grant BD (2010) EHBP-1 functions with RAB-10 during endocytic recycling in *Caenorhabditis elegans*. Mol Biol Cell 21:2930–2943.

Shikanai M, Yuzaki M, Kawauchi T (2018) Rab family small GTPases-mediated regulation of intracellular logistics in neural development. Histol Histopathol 33:765–771.

Shimada A, et al. (2007) Curved EFC/F-BAR-domain dimers are joined end to end into a filament for membrane invagination in endocytosis. Cell 129: 761–772.

Siri SO, Rozés-Salvador V, de la Villarmois EA, Ghersi MS, Quassollo G, Pérez MF, Conde C (2020) Decrease of Rab11 prevents the correct dendritic arborization, synaptic plasticity and spatial memory formation. Biochim Biophys Acta Mol Cell Res 1867:118735.

Taylor CA, Yan J, Howell AS, Dong X, Shen K (2015) RAB-10 regulates dendritic branching by balancing dendritic transport. PLoS Genet 11:e1005695.

Tröger J, Seemann E, Heintzmann R, Kessels MM, Qualmann B (2022) Spinal cord synaptic plasticity by GlyRβ release from receptor fields and syndapin I-dependent uptake. J Neurosci 42:6706–6723.

Wang P, Liu H, Wang Y, Liu O, Zhang J, Gleason A, Yang Z, Wang H, Shi A, Grant BD (2016) RAB-10 promotes EHBP-1 bridging of filamentous actin and tubular recycling endosomes. PLoS Genet 12:e1006093.

Wang Q, Navarro MV, Peng G, Molinelli E, Goh SL, Judson BL, Rajashankar KR, Sondermann H (2009) Molecular mechanism of membrane constriction and tubulation mediated by the F-BAR protein Pacsin/Syndapin. Proc Natl Acad Sci U S A 106:12700–12705.

Wolf D, Hofbrucker-MacKenzie SA, Izadi M, Seemann E, Steiniger F, Schwintzer L, Koch D, Kessels MM, Qualmann B (2019) Ankyrin repeat-containing N-Ank proteins shape cellular membranes. Nat Cell Biol 21: 1191–1205.

Zou W, Yadav S, DeVault L, Nung Jan Y, Sherwood DR (2015) RAB-10-dependent membrane transport is required for dendrite arborization. PLoS Genet 11:e1005484.